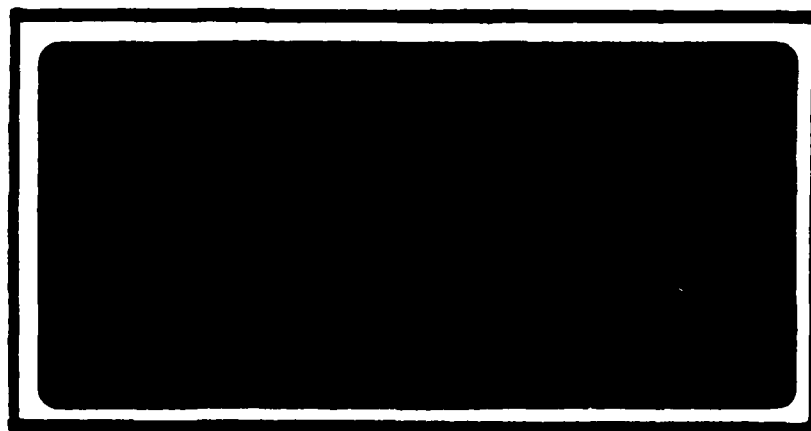


AD-A141 224



1



DTIC FILE COPY

DTIC
ELECTE
MAY 15 1984

S
B

DEPARTMENT OF THE AIR FORCE
AIR UNIVERSITY

AIR FORCE INSTITUTE OF TECHNOLOGY

Wright-Patterson Air Force Base, Ohio

DISTRIBUTION STATEMENT A

Approved for public release
Distribution Unlimited

84 05 14 117

PII Redacted

AFIT/GAE/AA/83D-22

EFFECTS OF NOZZLE AND GRID
ACCELERATION OF CORONA WIND ON COOLING
OF A VERTICAL FLAT PLATE

THESIS

Michael E. Stefkovich
Major, USAF

AFIT/GAE/AA/83D-22

Approved for public release; distribution unlimited

DTIC
ELECTE
MAY 15 1984
B

AFIT/GAE/AA/83D-22

EFFECTS OF NOZZLE AND GRID ACCELERATION
OF CORONA WIND ON COOLING OF
A VERTICAL FLAT PLATE

THESIS

Presented to the Faculty of the School of Engineering
of the Air Force Institute of Technology
Air University
In Partial Fulfillment of the
Requirements for the Degree of
Master of Science in Aeronautical Engineering

Michael E. Stefkovich
Major, USAF

December 1983

Approved for public release; distribution unlimited

Preface

This report describes the experimental investigation of the effects of nozzle and grid acceleration of a corona wind on cooling of a vertically suspended, heated, flat plate in air. Although much work has been done previously on corona wind cooling effects, only minimal work has been accomplished using corona wind accelerating devices.

Two types of emitter probes, a nineteen point emitter and a stretched wire emitter, as well as a variable nozzle with a removeable grid accelerator were designed, constructed, and used during the investigation.

The multipoint emitter was tested with a variable nozzle to determine the effect on convective heat transfer from a heated plate. Nozzle position, nozzle inlet/outlet area, and plate-to-emitter distances were varied. Results were compared with emitter (without nozzle) forced cooling and free convection cooling of the plate.

The stretched wire emitter was tested, with a grid accelerator attached to the variable nozzle, to determine the effect on convective heat transfer from the plate. Results were again compared to emitter (without nozzle) cooling and free convection cooling of the plate.

I wish to express my appreciation to Professor Milton E. Franke my thesis advisor, Professor James E. Hitchcock and Professor Wesley R. Cox for their timely suggestions and expert advice. Thanks are also due to Mr. Carl Shortt and the superbly capable members of the AFIT shop, for their practical advice and expert fabrication of required test apparatus.

Finally, I wish to thank my best friend: Lt Steven L. Pauletti
for his moral support and encouragement.

Michael E. Stefkovich

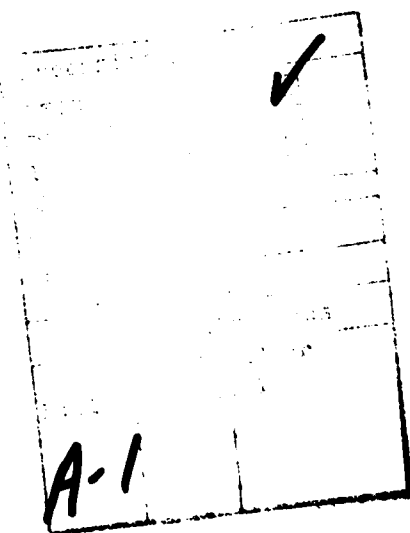


Table of Contents

	Page
Preface	ii
List of Figures	vi
List of Symbols	ix
Abstract	xii
I. Introduction	1
Objective	2
Approach	2
II. Experimental Apparatus	4
Heated Vertical Test Plate	4
Interferometer and Camera System	5
High Voltage System (DC)	5
Low Voltage System (AC)	5
Thermocouple System	6
Emitter Devices	6
Variable Nozzle and Grid Accelerator	7
III. Experimental Procedures	9
Interferometer Method	9
Energy Balance Method	10
Calibration Techniques	11
IV. Data Analysis	12
Interferometer Method Calculation Procedure	12
Empirical Method Calculation Procedure	12
Radiant Heat Transfer Calculation	13
Energy Balance Method Calculation Procedure	14
V. Results	17
Free Convection Heat Transfer No Applied Field	17
Baseline Results Test Apparatus A and B	17
Apparatus C	19
Apparatus D	20
Comparison of Local Area Cooling to Entire Front Surface Cooling of the Plate	22

	Page
VI. Conclusions	24
VII. Recommendations	25
Appendix I: Typical Properties of Test Plate Material . .	61
Appendix II: Typical Properties of Thermocouple Epoxy, "Omegabond 101"	62
Appendix III: VAX 11/780 Digital Computer Program	63
Appendix IV: Equipment List and Specifications	67
Bibliography	69
Vita	71

List of Figures

Figure	Page
1. Ducted Probe Configuration Used by Shannon and Pogson	27
2. Schematic Representation of Test Apparatus Configurations	28
3. Overall View of Test Apparatus	29
4. View of Instrumentation and Power Supply	29
5. View of Test Section	30
6. View of Heated Plate with Back Section Removed Showing Heater Elements	31
7. Plate Division by Element and Coordinate System as Viewed from Front Plate Surface	31
8. High Voltage System Wiring Diagram without Grid Accelerator	32
9. High Voltage System Wiring Diagram with Grid Accelerator	33
10a. Low Voltage System Wiring Diagram	34
10b. Low Voltage System Wiring Diagram	35
11. Thermocouple System Wiring Diagram	36
12. Front Surface Thermocouple Location	37
13. View of Emitters	38
14. View of Test Apparatus C	39
15. View of Test Apparatus D	39
16. Interference Photographs Showing the Initial Effect of an Electric Field on the Boundary Layer of a Vertical Plate for a Stretched Wire and a Multipoint Emitter	40

Figure	Page
17. Effect of Electric Field on the Ratio \bar{h}/\bar{h}_0 for the Stretched Wire Emitter at Various Plate-to-Emitter Distances ζ_e	41
18. Current, Voltage Relationship for the Stretched Wire Emitter at Various Plate-to-Emitter Distances ζ_e	42
19. Interference Photographs Showing the Effects of an Electric Field on the Thermal Boundary Layer of a Vertical Plate Using the Stretched Wire Emitter at Constant Plate-to-Emitter Distance ($\zeta_e = 1.0$ in.) . .	43
20. Effect of Electric Field on the Ratio \bar{h}/\bar{h}_0 for the Multipoint Emitter at Various Plate-to-Emitter Distances ζ_e	45
21. Current, Voltage Relationship for the Multipoint Emitter at Various Plate-to-Emitter Distances ζ_e . .	46
22. Interference Photographs Showing the Effects of an Electric Field on the Thermal Boundary Layer of a Vertical Plate Using the Multipoint Emitter at Constant Plate-to-Emitter Distance ($\zeta_e = 1.0$ in.) . .	47
23. Effect of Nozzle Area Ratio A_e/A_1 on the Ratio \bar{h}/\bar{h}_0 for the Stretched Wire Emitter and Grid Accelerator	49
24. Plate-to-Emitter Distance ζ_e Required to Maintain Constant Field Power ($P=0.545$ w) for Various Nozzle Area Ratios A_e/A_1 Using the Stretched Wire Emitter and Grid Accelerator	49
25. Interference Photographs Showing the Effects of an Electric Field on the Thermal Boundary Layer of a Vertical Plate with Various Nozzle Area Ratios A_e/A_1 and Grounded Grid Accelerator ($\zeta_n = 1.0$ in.) Using the Stretched Wire Emitter	50
26. Effect of Varying Nozzle Area Ratio A_e/A_1 on the Ratio \bar{h}/\bar{h}_0 with the Multipoint Emitter	52
27. Interference Photographs Showing the Effects of an Electric Field on the Thermal Boundary Layer of a Vertical Plate with Various Nozzle Area Ratios A_e/A_1 Using the Multipoint Emitter	53

Figure	Page
28. Effect of Varying Plate-to-Nozzle Distance ζ_n on the Ratio \bar{h}/\bar{h}_0 with the Multipoint Emitter Fixed at $\zeta_e = 1.0$ in. and the Nozzle Area Ratio Fixed at $A_e/A_i = 0.596$	55
29. Interference Photographs Showing the Effects of an Electric Field on the Thermal Boundary Layer of a Vertical Plate for Various Nozzle-to-Plate Distances ζ_n with Nozzle Area Ratio Constant ($A_e/A_i = 0.596$) Using the Multipoint Emitter ($\zeta_e = 1.0$ in.)	56
30. Effect of Varying Plate-to-Emitter Distance ζ_e on the Ratio \bar{h}/\bar{h}_0 for the Multipoint Emitter with Nozzle	58
31. Interference Photographs Showing the Effects of an Electric Field on the Thermal Boundary Layer of a Vertical Plate at Various Plate-to-Emitter Distances ζ_e Using the Multipoint Emitter	59
32. Source Program for Use with the VAX 11/780 Computer	64
33. Typical Input Data File	65
34. Typical Output Data File	66

List of Symbols

<u>Symbol</u>	<u>Definition</u>	<u>Units</u>
A	Area	ft ²
a	Current, DC	amp
A_e/A_i	Nozzle exit to inlet area ratio	--
C_p	Specific heat at constant pressure	Btu/lbm F
E	Electrical potential, AC	volt
F_{wa}	Radiant interchange factor	--
g	Acceleration due to gravity, 32.2	ft/sec ²
G_r	Grashof number $g\beta\Delta T x^3/\nu^2$	--
h	Local convection heat transfer coefficient (averaged in z direction)	Btu/hr ft ² F
\bar{h}	Average convection heat transfer coefficient	Btu/hr ft ² F
\bar{h}^*	Average convection heat transfer coefficient obtained with multipoint emitter without nozzle (P=0.545 w, $\zeta_e=1.0$ in.)	Btu/hr ft ² F
I	Current, AC	amp
k	Thermal conductivity	Btu/hr ft F
\bar{N}_u	Average Nusselt number, hx/k	--
P	Electric field power	watt
P_{lv}	Low voltage input power to plate heating elements	watt
P_r	Prandtl number, $\mu C_p/k$	--
Q	Heat transfer rate	Btu/hr
R	Electrical resistance	ohm

<u>Symbol</u>	<u>Definition</u>	<u>Units</u>
S	Plate height	in.
T	Temperature	F, R
ΔT	Temperature difference, $T_w - T_a$	F
V	Electric field potential, DC	kV
x	Distance along plate (vertical)	in.
y	Distance normal to plate	in.
z	Lateral distance along plate (horizontal)	in.
β	Thermal coefficient of volume expansion	1/F
ϵ	Emissivity for radiation	--
ζ_e	Plate-to-emitter distance	in.
ζ_n	Plate-to-nozzle distance	in.
μ	Dynamic viscosity	lbm/ft hr
ν	Kinematic viscosity	ft ² /hr
ρ	Fluid density	lbm/ft ³
σ	Stefan-Boltzmann constant, 0.1714×10^{-8}	Btu/hr ft ² R ⁴

Subscripts

a	Ambient
b	Back plane of plate
c	Convection
e	Emitter
j	Plate heater element
l	Losses through ends
n	Nozzle
o	No field applied

Subscripts

r	Radiation
t	Total
w	Front plane of plate

Abstract

Several experiments were conducted to determine the effect of nozzle and grid acceleration of a corona wind on the free convection heat transfer rate of a vertically mounted heated flat plate. The plate was maintained at ground potential and was suspended in a Mach-Zehnder interferometer. A positively charged stretched wire emitter and nineteen point emitter were used. Baseline tests were conducted to determine the changes in plate convective heat transfer rate attainable at various field power settings, and plate-to-emitter distances.

A two dimensional variable area convergent nozzle constructed of wood and plexiglas was used to accelerate the flow of the corona wind toward the plate. Nozzle inlet/exit area, plate-to-nozzle distance and plate-to-emitter distance was varied. A grid accelerator composed of an aluminum screen mesh was attached across the exit area of the convergent nozzle and was maintained at ground potential.

Plate heat transfer rates were determined from energy balance measurements and interferometer photographs. Results indicated that the nozzle and grid accelerator coupled with either emitter did not improve upon overall plate heat transfer rates obtained in baseline tests. On the contrary, heat transfer rates for individual plate sections were improved using the multipoint emitter and nozzle.

I. Introduction

Many experimental studies have been conducted regarding the effects of electrostatic fields on heat transfer rates. The electrostatic field effect, variously known as the electric wind or corona wind, refers to the movement of gas induced by the repulsion of ions from the vicinity of a high voltage discharge electrode (1).

Velkoff (2) was one of the first to investigate these effects on heat transfer under free convection from a flat plate. Marco and Velkoff (3) later demonstrated that the observed increase in convective heat transfer rate was due to the corona wind stream impinging on the heated plate, rather than due to electric field or thermal field gradient interactions. O'Brien and Shine (4) extended Velkoff's work to include the effect of pressure and type of gas on corona cooling. Franke (5) was able to produce improved convective cooling of a heated vertical plate by inducing counterrotating vortices resulting from a corona wind established between a set of alternately charged wires aligned vertically on the surface of a heated plate. Effects of voltage, probe spacing, and probe configuration on rate of convection cooling resulting from corona wind was further investigated by Demorest and Gause (6).

All of these investigations involved the cooling of a heated plate with a discharge electrode (emitter) composed of a single or multiple set of stretched wire or multiple point electrodes. Shannon and Pogson (7), however, studied the effect of directing the corona wind by using a ducted probe device (Fig. 1).

Objective

This study was initiated to experimentally investigate the effects of nozzle and grid acceleration of a corona wind on the convective heat transfer rate of a vertical, flat, heated plate in air. Although the forces involved with corona discharge are in general small, it appeared possible to use a two dimensional convergent nozzle and grid accelerator to accelerate the flow of air and ions from an emitter to a grounded heated plate. The objective of this study was to set up the conditions of corona cooling and then compare the unaccelerated cooling with the nozzle and grid accelerated cooling. Heat transfer results were obtained qualitatively with the interferometer and quantitatively through an energy balance method. No attempt was made to analytically model the highly complicated interrelation of free convection flows and the corona wind.

Approach

The investigation was divided into four parts:

1. The measurement of convective heat transfer rate from a heated plate with no applied high voltage electric field.
2. The determination of baseline convective heat transfer rates with multipoint and stretched wire emitters.
3. The comparison of the free convection and baseline convective heat transfer rates obtained using a stretched wire emitter (without nozzle or grid accelerator) with convective heat transfer rates obtained using a nozzle and grid accelerated stretched wire emitter.

4. The comparison of the free convection and baseline convective heat transfer rates obtained using a multipoint emitter (without nozzle or grid accelerator) with convective heat transfer rates obtained using a nozzle accelerated multipoint emitter.

II. Experimental Apparatus

The heat transfer rate from a vertically suspended heated plate was investigated using a Mach-Zehnder type interferometer and an energy balance method. The primary components of the experimental apparatus included: a heated vertical test plate, a Mach-Zehnder interferometer and camera system, a high voltage system (DC), a low voltage system (AC), a thermocouple system, emitter devices, and a variable nozzle/grid accelerator. Various test apparatus configurations used during the experiment are depicted schematically in Fig. 2. Figure 3 shows the overall test apparatus arrangement, while Fig. 4 shows the instrumentation and power supply.

Heated Vertical Test Plate

An electrically-heated aluminum plate (10 x 10 x 0.50 in.) was suspended vertically in the test section of a Mach-Zehnder interferometer (Fig. 5). The plate was constructed of 2024 aluminum. Pertinent specifications of 2024 aluminum are presented in Appendix I. The plate consisted of two sections. The front section (10 x 10 x 3/8 in.) was machined on its inner side, allowing for internal placement of heating elements (Fig. 6) and thermocouples. The outer plane surface of the front section was machined to provide a flat smooth surface. The back section of the plate (10 x 10 x 1/8 in.) was solid 2024 aluminum with holes drilled to allow mating of the two plate sections. Small tabs were attached to opposite edges of the plate to allow for alignment of the plate with the light path of the interferometer. The plate was partitioned into seven separately heated elements (Fig. 7).

Interferometer and Camera System

A Mach-Zehnder type interferometer (Fig. 3) with 8 in. optics and horizontal light path was used to observe the thermal boundary layer near the front surface of the heated plate. The interferometer employed a 100 watt mercury vapor light source. This light source was filtered with a Wratten No. 77A filter resulting in a monochromatic light of wavelength 5461 \AA . Fringe patterns obtained from the interferometer were recorded with a Polaroid Graflex camera using type 42 and 47 Polaroid high speed film.

High Voltage System (DC)

The high voltage system (Fig. 8,9) was used to establish and measure a high voltage potential (electric field) across the air gap between the emitter and the heated plate. A direct current power supply (0-30 kV, 0-35 ma) applied a positive charge to the emitter relative to the heated plate. The heated plate was maintained at ground potential. Voltage across the emitter/plate air gap was measured using a Sensitive Research Instrument Corp. electrostatic voltmeter (0-15 kV). Beldon high voltage wire type 8866, rated for 40 kV DC, was used for all high voltage leads.

Low Voltage System (AC)

The low voltage system (Fig. 10a,10b) supplied the alternating current (AC) electrical power used to heat the test plate. This system also allowed for metering of the input voltage and current to seven horizontally placed heater elements embedded in the heated plate. Figure 6 depicts heater placement. The coiled heater elements were made

of 0.0125 in. diameter nichrome wire covered with teflon tubing. Input voltage and current could be measured and varied separately for each of the seven independent heater elements.

Thermocouple System

The thermocouple system (Fig. 11) was used to measure the front and back plane surface temperature of the heated plate. Twenty-eight copper and constantan thermocouples (Honeywell type MN9B1N, 24 gage, nylon coated) were positioned with their hot junctions inside the heated plate. These hot junctions were located internally 1/16 in. from the front surface of the plate at locations depicted in Fig. 12. Each thermocouple junction was arc welded. Hot junctions were covered with "Omegabond 101" epoxy adhesive, which provided a thermally conductive yet electrically insulating coating. Properties of "Omegabond 101" are presented in Appendix II. A distilled water ice bath was used as the cold junction reference temperature for all thermocouples. A Honeywell "Electronik 16" strip chart recorder measured and recorded the output of twenty-four of the plate front surface thermocouples. The remaining four plate front surface thermocouples were connected to an automatic sequencing device and a DC digital millivoltmeter.

Two additional thermocouples were taped to the back surface of the plate. One thermocouple was placed in the free air of the test section at a location 12 ins. from the test plate.

Emitter Devices

Two separate emitter types were used during the investigation: a stretched wire emitter and a multipoint emitter (Fig. 13). Only one

type of emitter was used at a time.

The stretched wire emitter consisted of a 0.002 in. diameter nichrome wire pulled taut between two supporting copper electrodes. These electrodes were connected directly to the positive lead of the high voltage (DC) system. During operation the taut emitter wire formed a horizontal line parallel to the centerline of the front side of the heated plate.

The multipoint emitter consisted of nineteen $1/4 \times 0.002$ in. diameter nichrome wires mounted into 0.013 in. diameter holes drilled into the end of nineteen $4 \times 1/8$ in. diameter copper electrodes. When in use the copper electrodes were connected directly to the positive lead of the high voltage (DC) system.

A pulley (Fig. 5) was constructed to allow controlled movement of the emitter (either multipoint or stretched wire) in the y direction relative to the plate. A micrometer traversing mechanism (Fig. 5) which was connected to the pulley, was used to measure the plate-to-emitter distance z_e .

Variable Nozzle and Grid Accelerator

A two dimensional nozzle with variable inlet and exit area (Fig. 14,15) was mounted horizontally to the centerline of the test plate and formed a convergent nozzle about the emitter. The nozzle proper was made of two wooden wing-like structures. The supporting structure of the nozzle was constructed of plexiglass. The entire nozzle assembly could be moved in the y direction relative to the plate and the emitter.

An accelerating screen (grid accelerator) made of aluminum screen mesh could be mounted across the exit area of the nozzle (Fig. 2,14).

The wire mesh consisted of 29 gage aluminum wire interlaced into squares providing a 0.05 in. square opening between wires. When in use the grid accelerator was connected to the ground potential of the high voltage system. In this case, the heated plate was grounded directly to ground potential through a DC microammeter (Fig. 9).

III. Experimental Procedures

The heat transfer rate from the entire front surface of the heated plate was obtained using an interferometer method and an energy balance method. The test procedures and calibration techniques are described.

Interferometer Method

This method involved the use of interference photographs. Tests were made using test configurations depicted in Fig. 2.

First the heated plate was aligned with the light path of the interferometer using the small tabs attached to the opposite edges of the test plate. Liquid levels were used to align the top surface of the plate with the horizontal and the front surface of the plate with the vertical. Once plate alignment was attained, the emitter probe (either stretched wire or multipoint) was aligned with the plate. In either case the emitter was brought into contact with the front surface of the test plate. The emitter was then centered in the x, y, and z direction relative to the plate. Once probe-to-plate alignment was accomplished, the plate-to-emitter distance z_e was adjusted using the pulley and micrometer traversing devices. In the cases when the nozzle or nozzle and grid accelerator was used, the nozzle was aligned using the light of the interferometer.

Once all required alignments were completed, the seven input variable transformers (Fig. 10b) were adjusted separately to establish the desired plate-to-room temperature difference ΔT . In all tests this temperature difference was 50 F. The interferometer was adjusted to the

infinite fringe setting. After the desired plate-to-room temperature stabilized, an interference photograph was made. The high voltage field power was then applied across the emitter/plate air gap. After application of the field power, the low voltage input to each of the seven plate heater elements was adjusted individually to re-establish the original plate-to-room temperature difference of 50 F. An interference photograph was taken at this new stabilized condition. Ambient room temperature was recorded periodically during the experiment. Barometric pressure and room humidity was recorded as the test plate was initially heating. Several tests with various field power settings and test apparatus configurations (Fig. 2) were made.

Energy Balance Method

The change of plate heat transfer rate, resulting from the corona wind, was determined by measuring the change of rate of energy input to the plate heaters required to re-establish the original plate-to-room temperature difference ΔT . By keeping ΔT constant, radiation heat transfer change was minimized and convective heat transfer change, as a result of corona wind, could be measured directly. This method was used for the test configurations A,B,C and D depicted in Fig. 2.

Specific test procedures for the energy balance method are described. Ambient room temperature and humidity were measured, and alignment procedures were accomplished as described in the interferometer method test procedures. Plate-to-ambient temperature difference was stabilized for a ΔT of 50 F. Input voltage and current to each of the seven plate heater elements were recorded. Emitter field power was then applied to the desired level. Plate heater power was adjusted using the

separate input variable transformers to re-establish the original ΔT . Input voltage and current to each of the seven plate heater elements was again recorded. This procedure was repeated for various field power conditions and apparatus configurations A,B,C and D (Fig. 2).

Calibration Techniques

The thermocouples used in the experiment were calibrated with a Fisher Scientific mercury thermometer. The thermocouples and mercury thermometer were heated simultaneously in a distilled water flask. For a temperature range of 70 to 135 F all thermocouples were within 1 F of the mercury thermometer. Thermocouples not meeting this tolerance were discarded.

Calibration of the strip chart recorder was accomplished using the Soltec programmable DC voltage/current generator. A precision micropot was used to vary the scale and range of the strip chart recorder. Once the scale and range of the recorder were adjusted using the micropot, known voltages were applied by the programmable voltage generator to calibrate the recorder. This calibration was rechecked with a portable potentiometer and was found to be within 1 F over the temperature range of 70 to 135 F.

All other meters were calibrated by the Precision Measurements Laboratory, Wright-Patterson AFB.

IV. Data Analysis

An interferometer method, empirical method, and an energy balance method were used to obtain the heat transfer rate from the entire front surface of the heated plate. The calculation used with each method is described.

Interferometer Method Calculation Procedure

Plate front wall temperatures T_w and convective heat transfer coefficients \bar{h}_o were computed in the normal way (8, 9). A traveling microscope, accurate to 0.001 cm, was used to measure the distance from the front plate plane to the first three interference fringes. Fringe measurements were repeated at intervals of 0.71 in., starting at the centerline of the plate, along the $\pm x$ direction. The total number of fringes was counted at each interval. O'Brien's computer program (10) was modified to operate on the AFIT VAX 11/780 computer and was used to compute the heat transfer coefficients and wall temperature along the plate (Appendix III). The calculation procedures involving the interferometer method were limited to free convection no applied field conditions only. When the field power was applied the individual interference fringes were unreadable, and only qualitative results were attained. The use of the interferometer for convective heat transfer measurements is discussed further in the results section.

Empirical Method Calculation Procedures

Determination of the average convective heat transfer coefficient \bar{h}_o for the entire front surface of the plate was also made using the

well-accepted empirical equation (11).

$$\bar{N}_u = 0.555 (G_r P_r)^{1/4} \quad (1)$$

where

$$\bar{N}_u = \frac{\bar{h}_o}{k} S \quad (2)$$

thus

$$\bar{h}_o = k \frac{(0.555)(G_r P_r)^{1/4}}{S} \quad (3)$$

Radiant Heat Transfer Calculation

The rate of heat transfer by radiation Q_r from both plane surfaces of the plate is given by

$$Q_r = \sigma A F_{wa} (T_w^4 - T_a^4) \quad (4)$$

Assuming the plane surfaces of the plate are small gray bodies surrounded by a large surface, F_{wa} is then equal to ϵ and

$$Q_r = \sigma A \epsilon (T_w^4 - T_a^4) \quad (5)$$

Values of emissivity for 2024 aluminum range from 0.035 to 0.070 (Appendix I). The 0.070 value for emissivity applies to polished 2024 aluminum, and was used for all computations. One can readily see from equation (5), that if the wall to ambient temperature is maintained constant and if the ambient temperature stays fairly constant (say ± 5 R), then the radiant heat transfer from the plate plane surfaces will be relatively constant.

Energy Balance Method Calculation Procedure

To obtain the relative effects of the various test configurations and field power settings on the convective heat transfer rate of the plate, it was necessary to determine \bar{h}/\bar{h}_0 . The ratio \bar{h}/\bar{h}_0 being defined as the ratio of the average coefficient of heat transfer of the entire front plane surface of the plate (with field applied) to that without field applied. For clarity, \bar{h}/\bar{h}_0 for a particular element front plate surface will be subscripted by the particular element numerical designator (i.e. \bar{h}_3/\bar{h}_{03} refers to element 3 as shown in Fig. 4). The method for determining \bar{h}/\bar{h}_0 presented here follows the method used by Franke (12) with only slight modification.

The expression for the rate of heat transfer by convection for the front plane surface of the plate is

$$Q_{cw} = \bar{h}A\Delta T \quad (6)$$

The ratio of Q_{cw}/Q_{cow} using equation (1) yields

$$\frac{Q_{cw}}{Q_{cow}} = \frac{\bar{h}A\Delta T}{\bar{h}_0A\Delta T} \quad (7)$$

If the area A and temperature difference ΔT are constant,

$$\frac{\bar{h}}{\bar{h}_0} = \frac{Q_{cw}}{Q_{cow}} \quad (8)$$

The rate of heat transfer at any given time may be expressed as

$$Q_{cw} = Q_{cow} + \Delta Q_{cw} \quad (9)$$

substituting equation (8) into (9) yields

$$\frac{\bar{h}}{\bar{h}_o} = 1 + \frac{\Delta Q_{cw}}{Q_{cow}} \quad (10)$$

Either equation (8) or (10) can be used to determine \bar{h}/\bar{h}_o . The total heat transfer rate from all surfaces of the plate Q_t is equal to the sum of plane surface convection and radiation heat transfer rates plus the losses from the plate edges.

$$Q_t = Q_{cw} + Q_{cb} + Q_r + Q_l \quad (11)$$

The change in total heat transfer rate from the plate ΔQ_t from free convection to field applied convection is given by

$$\Delta Q_t = \Delta Q_{cw} + \Delta Q_{cb} + \Delta Q_r + \Delta Q_l \quad (12)$$

If the changes in heat transfer rate ΔQ_{cb} , ΔQ_r and ΔQ_l are small

$$\Delta Q_t = \Delta Q_{cw} \quad (13)$$

Under steady conditions, the rate of energy input to the plate heater elements P_{lv} is equal to the total heat transfer rate from the plate Q_t . The total heat transfer rate from the plate was obtained by measuring the voltage and current to the individual plate heaters and computed using the relations

$$Q_t = P_{lv} = \sum E_j I_j \quad j = 1, 7 \quad (14)$$

or

$$Q_t = P_{lv} = \sum I_j^2 R_j \quad j = 1, 7 \quad (15)$$

The subscript j denotes the particular plate heater element. Voltage

drop due to the resistance of the heater element lead wires, although small, was accounted for in the computation of P_{lv} . It follows that the change in total heat transfer rate ΔQ_t is equal to the change in plate heater power input ΔP_{lv} . This and equation (13) yields

$$\Delta Q_t = \Delta P_{lv} = \Delta Q_{cw} \quad (16)$$

substituting equations (7) and (16) into (5) gives the result

$$\frac{\bar{h}}{\bar{h}_o} = 1 + \frac{\Delta P_{lv}}{\bar{h}_o A (T_w - T_a)} \quad (17)$$

V. Results

Free Convection Heat Transfer No Field Applied

The free convection heat transfer rate with no applied field for the entire front surface of the plate was determined to be 28.12 Btu/hr using the interferometer method and 27.83 Btu/hr using the described empirical method. This result was for a plate temperature of 127 F and a ΔT of 50 F.

Baseline Results Test Apparatus A and B

By testing both the stretched wire emitter (apparatus A) and the multipoint emitter (apparatus B) without nozzle or grid accelerator, baseline values of \bar{h}/\bar{h}_0 for the entire front surface of the plate at various field power settings P were attained.

Figure 16 shows the initial effect of the corona wind on the thermal boundary layer observed while using the stretched wire emitter and then the multipoint emitter. No effect on the thermal boundary layer could be detected until a current was measured between the emitter and plate. Initial current flow occurred from 4-6 kV and varied depending on probe-to-plate distance. Thermal boundary layer "pull-out" as described by Velkoff (2) was noted at low field power (Fig. 16, photo 1). Velkoff postulated that the corona wind approaching the plate formed an upward and downward flow. The downward flow of the corona wind was working against the normal upward flowing convective stream along the plate. This interference resulted in the "pull-out" phenomena. Figure 16, photo 2 shows the markedly different effect on the boundary layer caused by the multipoint emitter at low field power. The boundary

layer located above the emitter was more unstable for the multipoint emitter than the boundary layer for the stretched wire emitter. It would appear that the corona wind flow caused by the multipoint emitter was more turbulent than that from the stretched wire emitter. This would account for less interactive effect on the rising convective stream for the multipoint emitter.

The effect of varying field power input P on \bar{h}/\bar{h}_0 using the wire emitter at various plate-to-emitter distances ζ_e is presented in Fig. 17. For the stretched wire emitter, \bar{h}/\bar{h}_0 was almost independent of plate-to-emitter distance and varied only with input field power. The relationship of field potential to current while using the stretched wire emitter is reflected in Fig. 18. Interferometer photographs (Fig. 19) show sequentially the initial start of boundary layer effect through the reduction in the thermal boundary layer thickness. A vortex (rotating counter-clockwise as viewed in Fig. 19, photo 2) formed below the horizontal line between the emitter and centerline of the plate. Vortex strength and reduction in boundary layer thickness increased as field power was increased.

Similar baseline results were obtained for the multipoint emitter. Figure 20 shows the effect of varying field power for different plate-to-emitter distances. A definite increase in \bar{h}/\bar{h}_0 occurred when ζ_e was changed from 0.5 in. to 1.0 in. This increase in \bar{h}/\bar{h}_0 continued for $\zeta_e = 1.25$ in. The relation of field potential to current while using the multipoint emitter is represented in Fig. 21. Interferometer photographs (Fig. 22) show the sequence of increased field power effects on the thermal boundary layer using the multipoint emitter. Once again an

initial boundary layer "pull-out" was observed (Fig. 22, photo 2) followed by the reduction in the boundary layer thickness at higher field power settings.

Comparison of Figs. 17 and 20 indicate that \bar{h}/\bar{h}_0 obtained while using the multipoint emitter was approximately equivalent to \bar{h}/\bar{h}_0 while using the stretched wire emitter when ζ_e was 0.5 in. Values of \bar{h}/\bar{h}_0 obtained with the multipoint emitter were notably higher than those obtained with the stretched wire emitter for the 1.0 in. and 1.25 in. plate-to-emitter distances.

All interferometer photographs taken had smooth interference lines. These smooth unbroken lines indicated a laminar flow between the emitter and plate.

Apparatus C

Apparatus C, stretched wire emitter with nozzle and grid accelerator (Figs. 2 and 14), was tested with a constant field power input of $P = 0.545$ w. Plate-to-nozzle distance was maintained constant at $\zeta_n = 1.0$ in. The plate-to-emitter distance ζ_e was varied according to Fig. 24 to maintain constant input power. The ratio of exit nozzle area to inlet nozzle area A_e/A_1 was then varied to determine the effect of the nozzle and grid accelerator combination on \bar{h}/\bar{h}_0 of the plate. Figure 23 illustrates this effect. The baseline values of \bar{h}^*/\bar{h}_0 obtained in baseline testing of the multipoint emitter were not achieved by the stretched wire emitter in combination with the nozzle and grid accelerator. Current flow was not recorded between the plate and ground at any time during this phase of testing. The absence of ion flow to the plate as well as increased overall plate-to-emitter

distances resulted in reduced \bar{h}/\bar{h}_0 values. Comparison of interference photographs (Fig. 25) for apparatus C and (Fig. 19, photos 3 and 4) for apparatus A confirm qualitatively these results. Figure 19, photo 4 depicts the reduction in the thermal boundary layer thickness obtained in baseline testing. Comparing that photo to Fig. 25 shows the effect of the nozzle with grid accelerator on the thermal boundary layer. Note the increasing curvature of the outermost interference pattern obtained as the nozzle area ratio was reduced. This increasing curvature indicates that the nozzle was directing the corona wind in a more narrow stream toward the plate as the nozzle area ratio was reduced. The vortex which had been observed during baseline testing of the stretched wire emitter was not observed during testing of apparatus C. The lower surface of the nozzle apparently formed a physical boundary that prevented the formation of the vortex. During apparatus C testing arcing became a problem as the nozzle area ratio was reduced at high field potentials (above 14 kV). This effect was attributed to an increased ion concentration in the reduced volume between the emitter and the grid accelerator.

Apparatus D

Apparatus D, multipoint emitter with nozzle, (Figs. 2 and 15) was tested in three phases, phase 1, 2, and 3. During all phases of testing apparatus D, an attempt was made to maintain field power constant. Scale limitations of the electrostatic voltmeter limited the ability to reset the same field power. Actual field power setting at each test point is presented in Figs. 26, 28, and 30.

Phase 1 testing of apparatus D was accomplished by varying nozzle

area ratio A_e/A_1 while maintaining plate-to-emitter and plate-to-nozzle distances constant ($\zeta_e = \zeta_n = 1.0$ in.). Figure 26 depicts the effect of varying nozzle area ratio on the ratio \bar{h}/\bar{h}_0 . Interferometer photographs (Fig. 27) show the various test cases and their effects on the thermal boundary layer. Figure 26, points 1-6 relate directly to Fig. 27, photos 1-6. The baseline cooling of the plate is indicated by \bar{h}^*/\bar{h}_0 in Fig. 26. Figure 22, photo 5 represents the interferometer photo of the reduction in thermal boundary layer thickness attained with the multipoint emitter without nozzle. Figure 26, points 2, 5 and 6 were photographs taken when the highest values of \bar{h}/\bar{h}_0 were obtained during phase 1 testing. Figure 27, photos 2, 5 and 6 indicate the greatest reduction in thermal boundary layer thickness over the widest area of the plate. Figure 27, photos 1, 3 and 4 do not indicate as much reduction in thermal boundary layer thickness and thus poorer plate cooling. Comparing all photographs of Fig. 27 to Fig. 22, photo 5 confirms the result that the unnozzled cooling was more effective than the nozzled cooling of the entire front plate surface. The vortex which had formed during baseline testing was not present during any of the phase 1 tests. The physical presence of the nozzle eliminated the vortex and thus reduced the values of overall plate cooling obtained.

Phase 2 testing of apparatus D was accomplished by selecting the nozzle area ratio $A_e/A_1 = 0.596$. Plate-to-nozzle distance ζ_n was varied while plate-to-emitter distance ζ_e was maintained at 1.0 in. The effect of varying ζ_n on the ratio \bar{h}/\bar{h}_0 is shown in Fig. 28. As the nozzle was moved away from the plate a rise in \bar{h}/\bar{h}_0 is indicated until a maximum \bar{h}/\bar{h}_0 was attained at $\zeta_n = \zeta_e = 1.0$ in. Again the maximum \bar{h}/\bar{h}_0

did not achieve \bar{h}^*/\bar{h}_0 which was obtained in baseline tests. Interference photographs (Fig. 29) show various test cases and reduction in the thermal boundary layer thickness. At $\zeta_n = 0.25$ the exit area of the nozzle was greater than the area formed between the nozzle and plate. This reduction in flow area at $\zeta_n = 0.25$ contributed to a lower \bar{h}/\bar{h}_0 .

Phase 3 testing of apparatus D was accomplished with the nozzle area ratio fixed ($A_e/A_1 = 0.596$) and plate-to-nozzle distance fixed ($\zeta_n = 1.0$ in.). Plate-to-emitter distance was varied from 0.25 to 1.5 in. The effect of varying plate-to-nozzle distance ζ_e on the ratio \bar{h}/\bar{h}_0 is represented in Fig. 30. The ratio \bar{h}/\bar{h}_0 increased rapidly until $\zeta_e = 1.0$ in. then leveled off from $\zeta_e = 1.0$ to 1.5 in. Interference photographs Fig. 31, qualitatively enhance these results by comparing boundary layer thickness at various plate-to-emitter distances. Figure 31, photos 1-6 relate directly to Fig. 30, points 1-6. Figure 30, points 1-4 indicate an increasing \bar{h}/\bar{h}_0 for the plate front surface. Figure 31, photos 1-4 reflect sequentially an increasing reduction in boundary layer thickness and thus an increasing heat transfer rate. Little change in boundary layer thickness can be detected between Fig. 31, photos 4-6. This correlates nicely with the leveloff of \bar{h}/\bar{h}_0 values in Fig. 30, points 4-6. The vortex noted in baseline testing was not present in phase 3 tests.

Comparison of Local Area Cooling to Entire Front Surface Cooling of the Plate

The question arises: Was local area cooling of the plate front surface improved using the nozzle and grid accelerator even though overall front plane surface cooling was not? Up to this point in the

results discussion, only entire front plane surface cooling has been addressed. Due to vertical heat transfer between heated elements of the plate, energy balance data taken for the individual elements were considered unuseable for determining local area cooling. Interferometer photographs; however, do indicate in some cases local area cooling at a given point on the plate was improved over baseline results. Comparing minimum thermal boundary layer thickness in Fig. 25 with that in Fig. 19, photo 4 it is apparent that apparatus C did not improve local area cooling. Measurements of minimum thermal boundary layer thickness for apparatus D tests indicate local area cooling was improved over local cooling indicated in Fig. 22, photo 5. Fig. 29, photo 4 and Fig. 31, photos 2-4 indicate improved local area cooling.

VI. Conclusions

Based on the results of this study the following conclusions are drawn:

1. No measurable effect on plate cooling occurred until a current was present between the emitter and plate or the emitter and grid accelerator. This condition was independent of field potential as long as current was not present. Interferometer photographs showed no noticeable boundary layer effect occurred until current flow.

2. The 19 point emitter was more effective than the stretched wire emitter in cooling the plate front surface when plate-to-emitter distances were greater than 0.5 in. At 0.5 in. plate-to-emitter distance the cooling effect of the two emitter types were approximately equivalent.

3. The stretched wire emitter with nozzle and grid accelerator did not cool the entire plate front surface as well as the stretched wire emitter alone. Ion flow to the plate was not required to effect plate cooling. This indicated that cooling of non-electrical conducting materials could be accomplished using the nozzle and grid accelerated corona wind.

4. Varying nozzle position, nozzle area ration and plate-to-emitter distance using the multipoint emitter did not increase cooling of the plate over that cooling attained with the multipoint emitter only.

5. The physical presence of the nozzle eliminated formation of a vortex near the lower surface of the plate.

VII. Recommendations

Further investigation of nozzle acceleration of corona wind should be done with different nozzle sizes. In particular nozzle planes with shorter chord length should be tested.

A study to obtain qualitative results from interferometer photographs should be made.

Grid accelerator configurations need further testing. The following parameters should be varied:

1. Grid-to-plate spacing
2. Grid opening dimension
3. Grid-to-nozzle spacing

Stacked arrays of multipoint emitters should be investigated.

Vertical heat transfer between plate elements should be reduced as much as possible to validate local area plate cooling.

FIGURES

Figs. 1 through 31

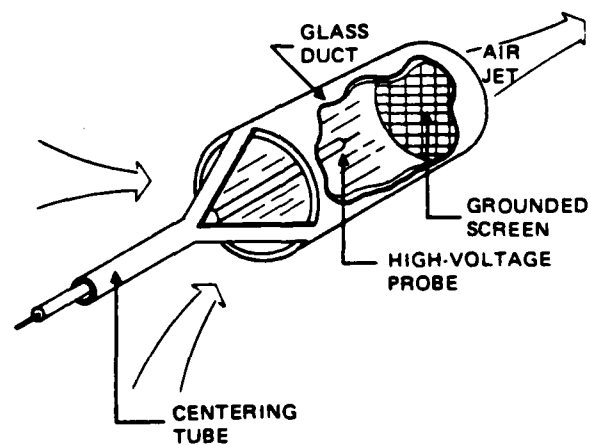


Fig. i. Ducted Probe Configuration Used by Shannon and Pogson (7)

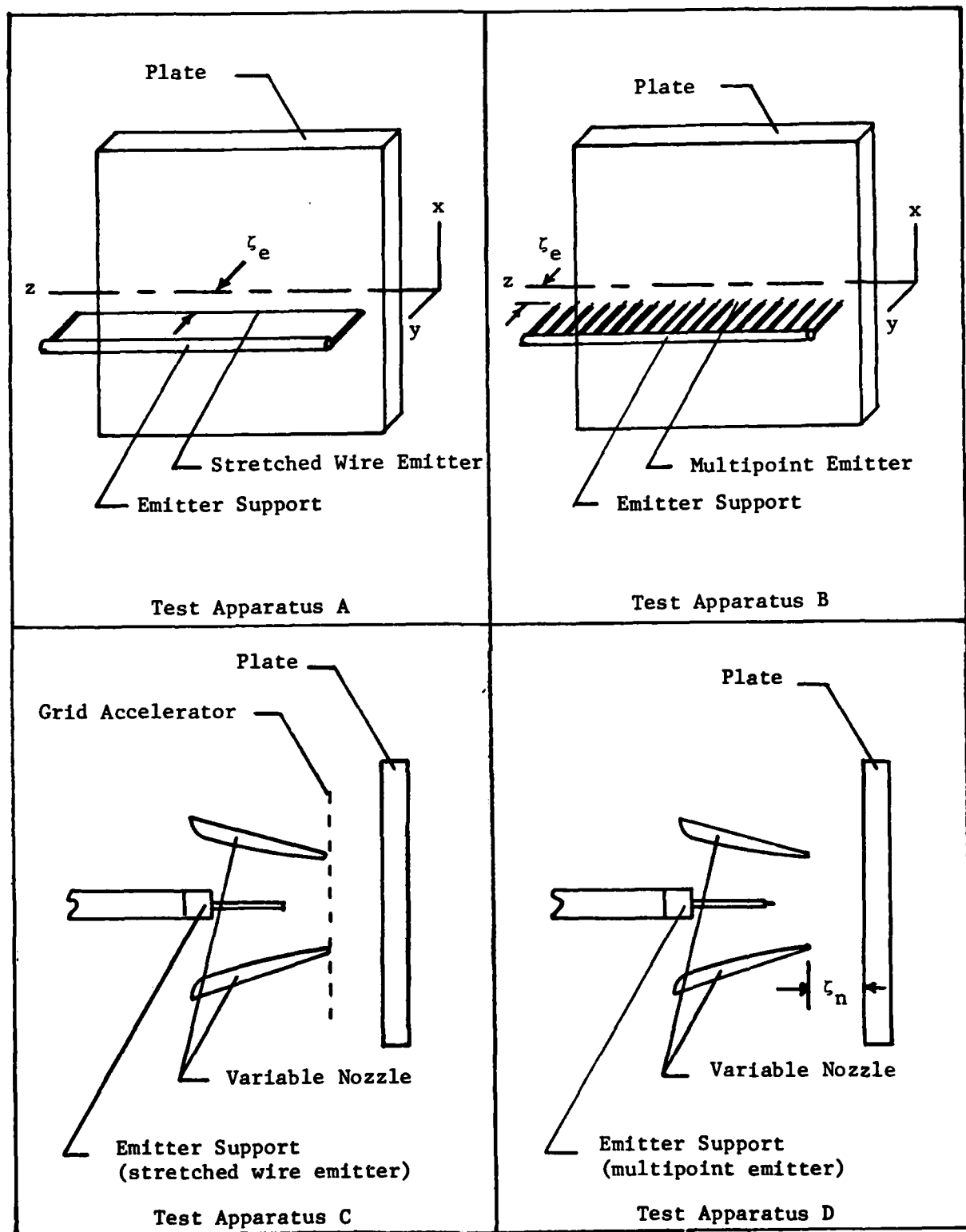


Fig. 2. Schematic Representation of Test Apparatus Configurations

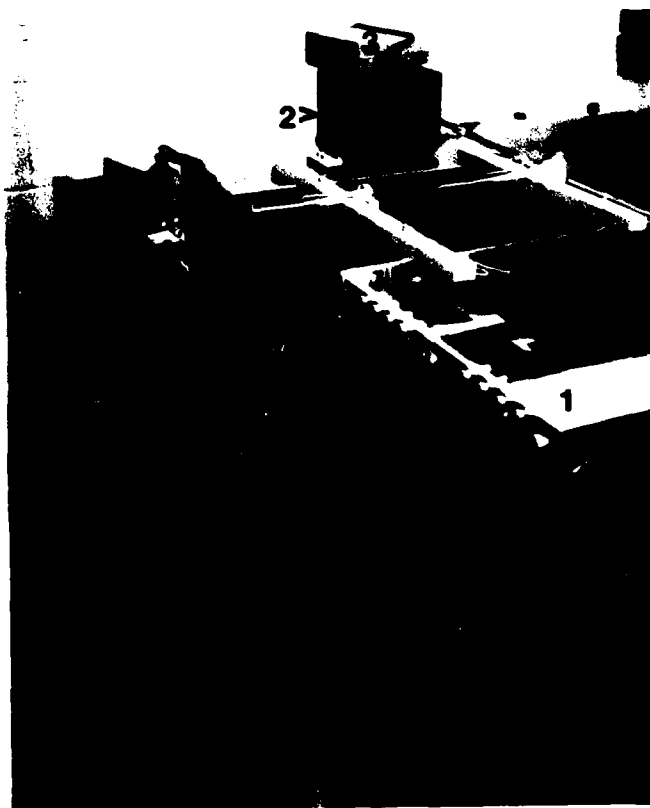


Fig. 3. Overall View of Test Apparatus

- (1) Optical Interferometer
- (2) Electrostatic Voltmeter
- (3) Digital Microammeter
- (4) Low Voltage Switch Box



Fig. 4. View of Instrumentation and Power Supply

- (1) Strip Chart Recorder
- (2) Ice Bath
- (3) Thermocouple Sequencer
- (4) Voltmeter
- (5) Ammeter
- (6) Voltmeter
- (7) High Voltage Power Supply
- (8) Wattmeter
- (9) Variable Transformers for Plate Heating Elements

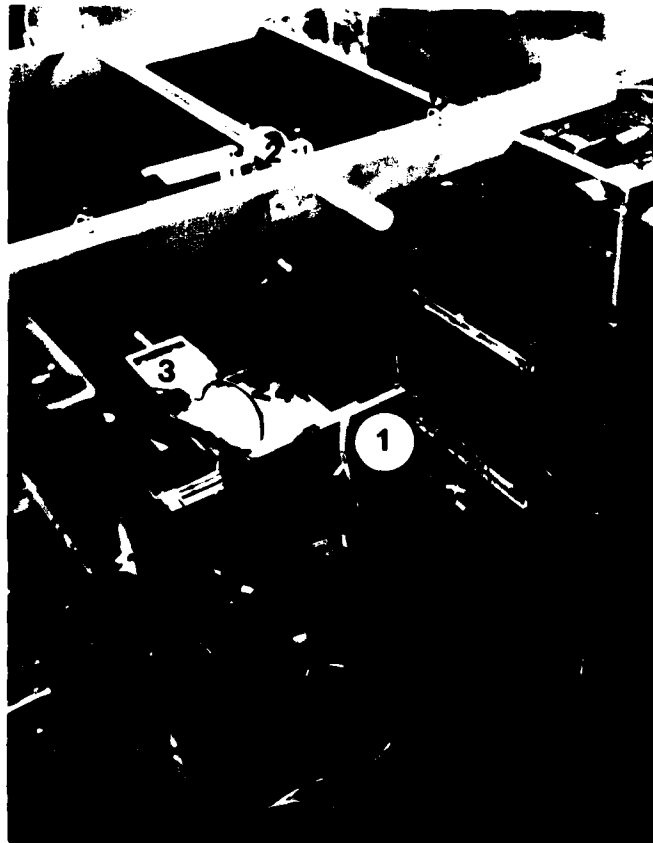


Fig. 5. View of Test Section

- (1) Heated Plate
- (2) Pulley Device
- (3) Traversing Device
- (4) High Voltage Lead

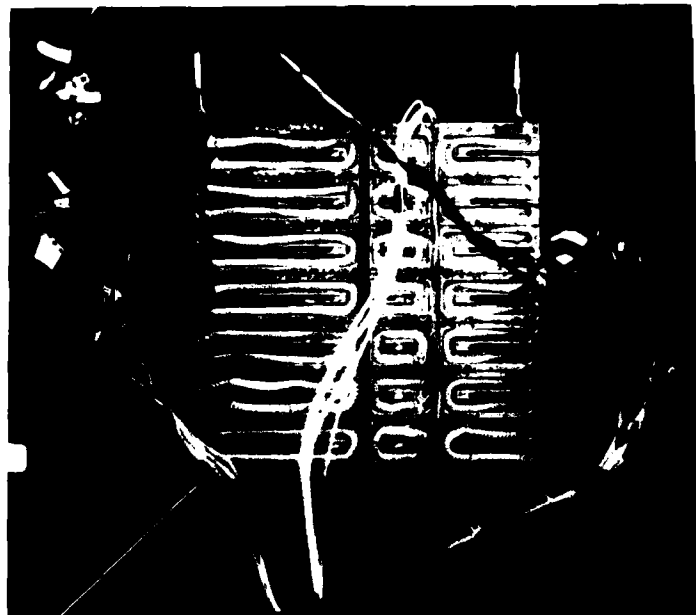


Fig. 6. View of Heated Plate with Back Section Removed Showing Heater Elements

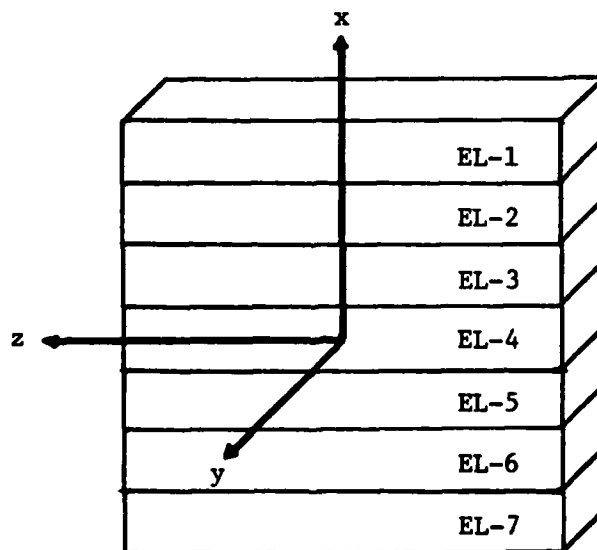


Fig. 7. Plate Division by Element and Coordinate System as Viewed from Front Plate Surface (EL - Element)

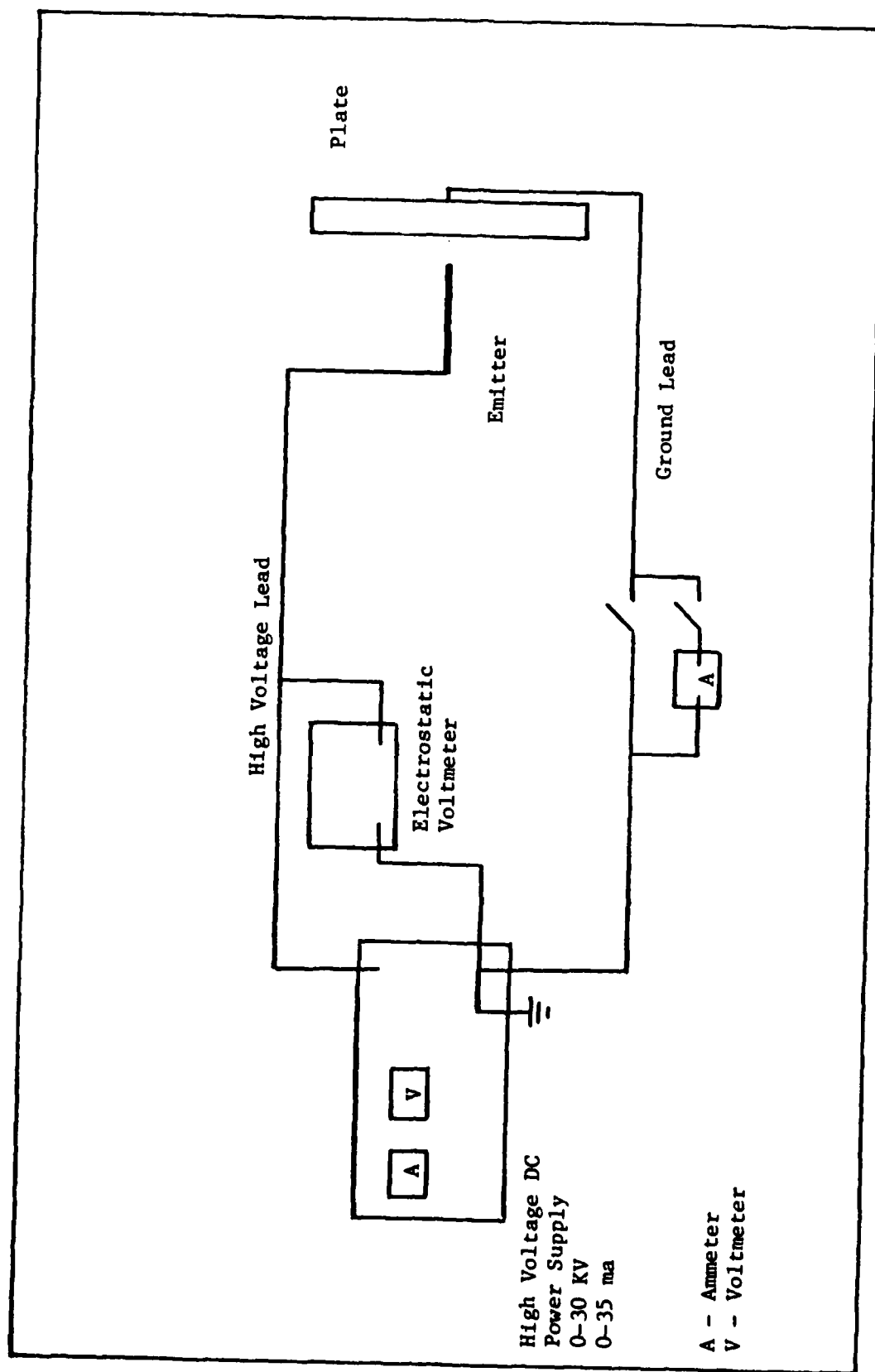


Fig. 8. High Voltage System Wiring Diagram Without Grid Accelerator

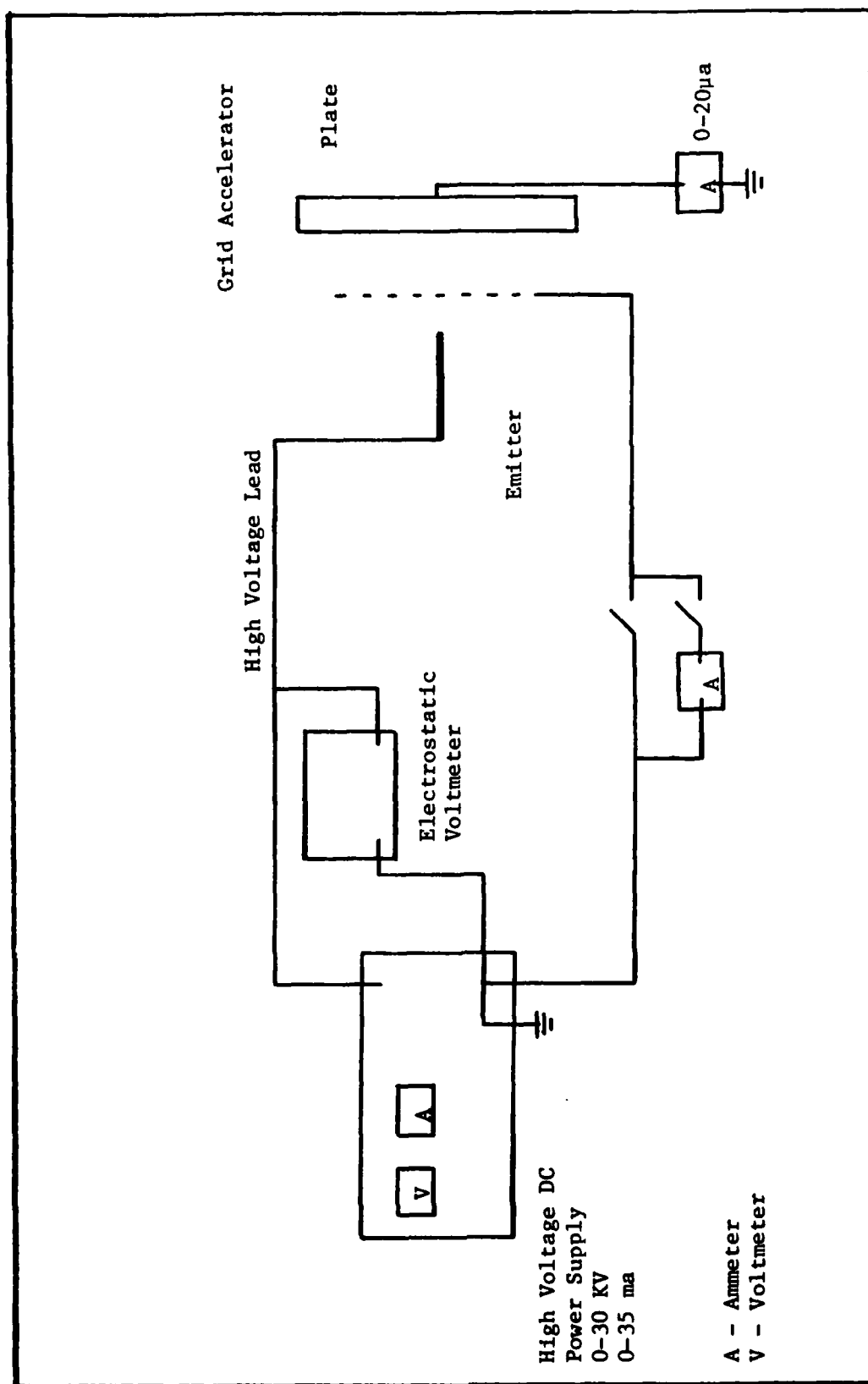


Fig. 9. High Voltage System Wiring Diagram with Grid Accelerator

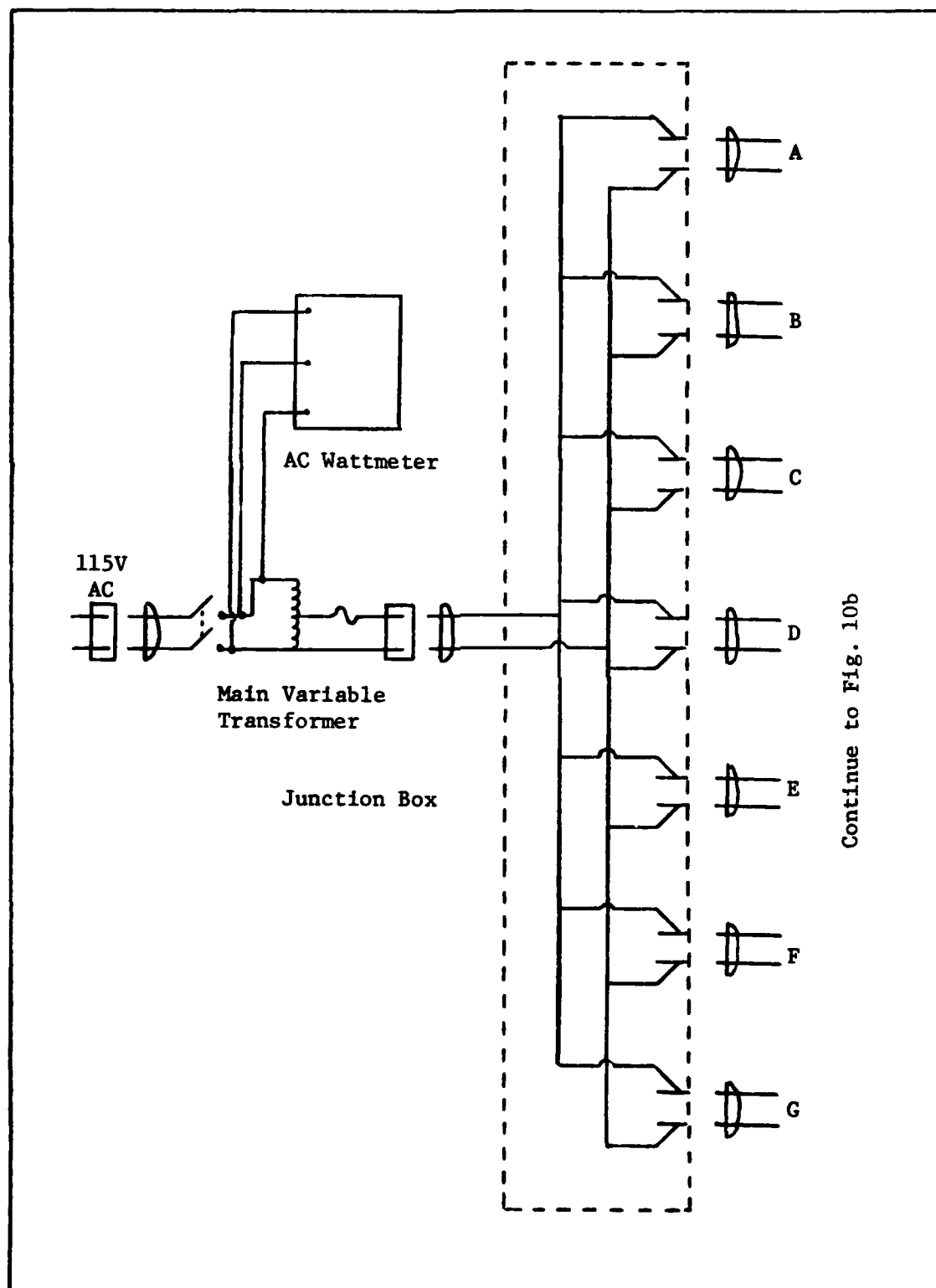


Fig. 10a. Low Voltage System Wiring Diagram

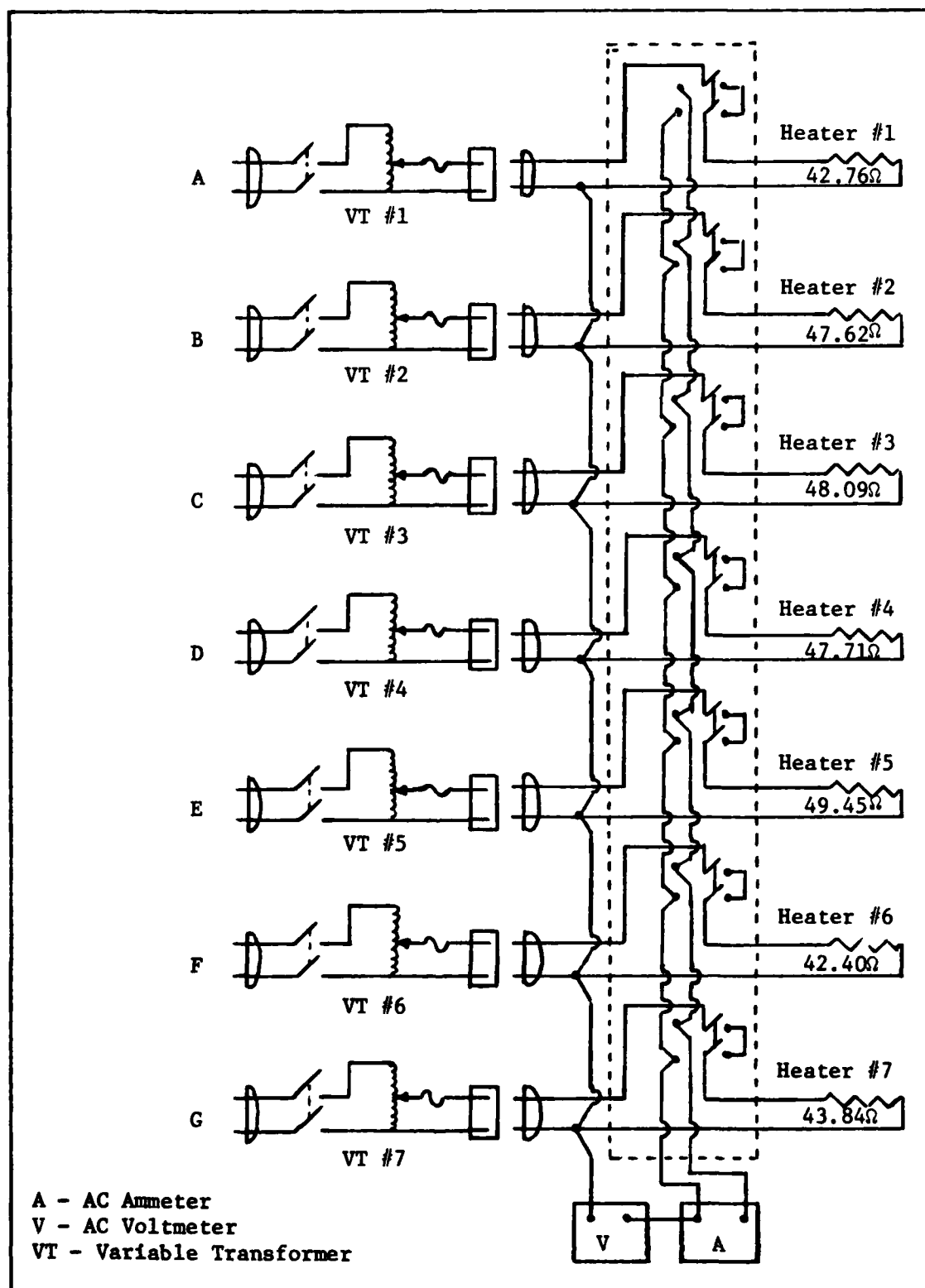


Fig. 10b. Low Voltage System Wiring Diagram

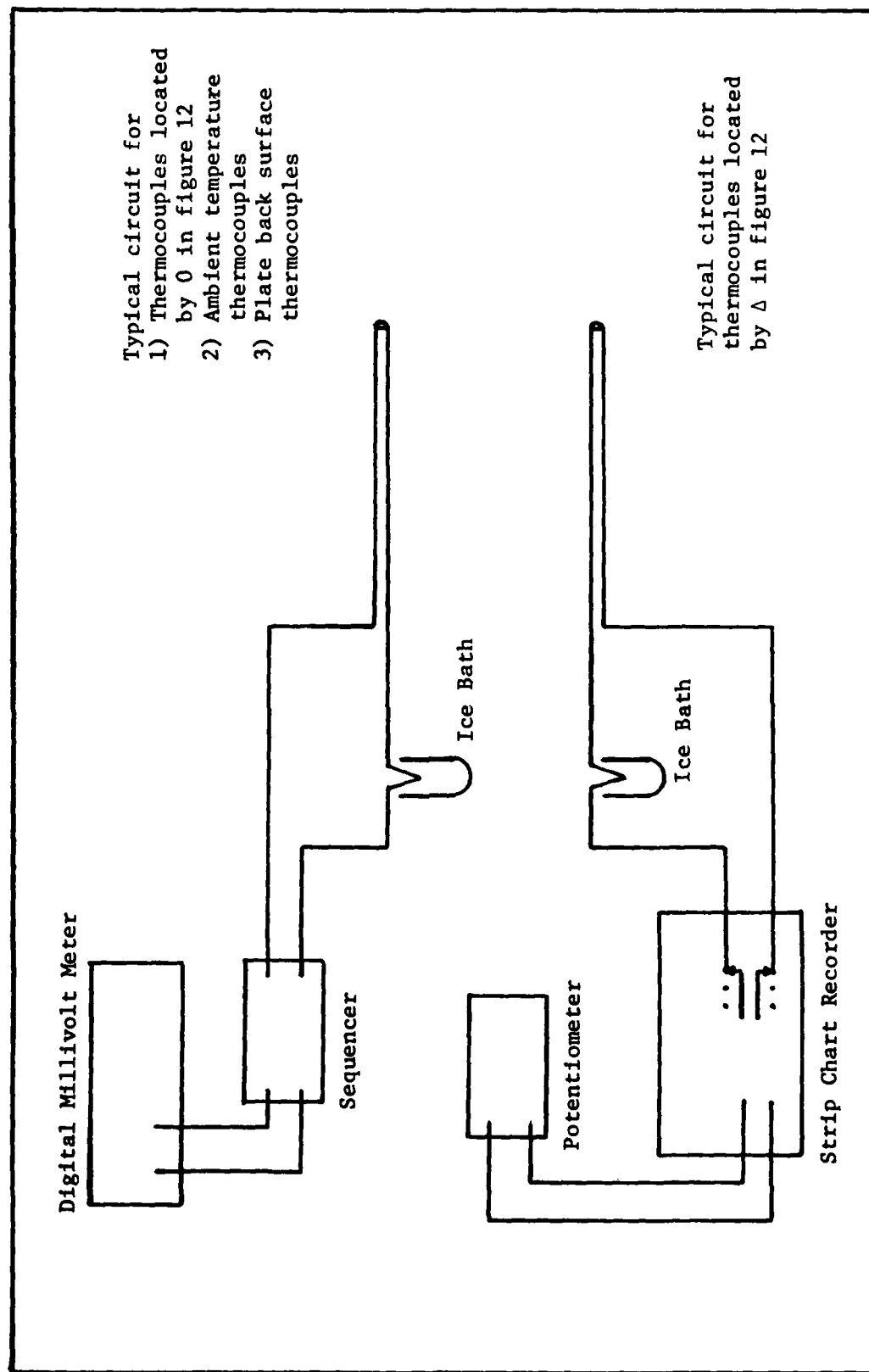
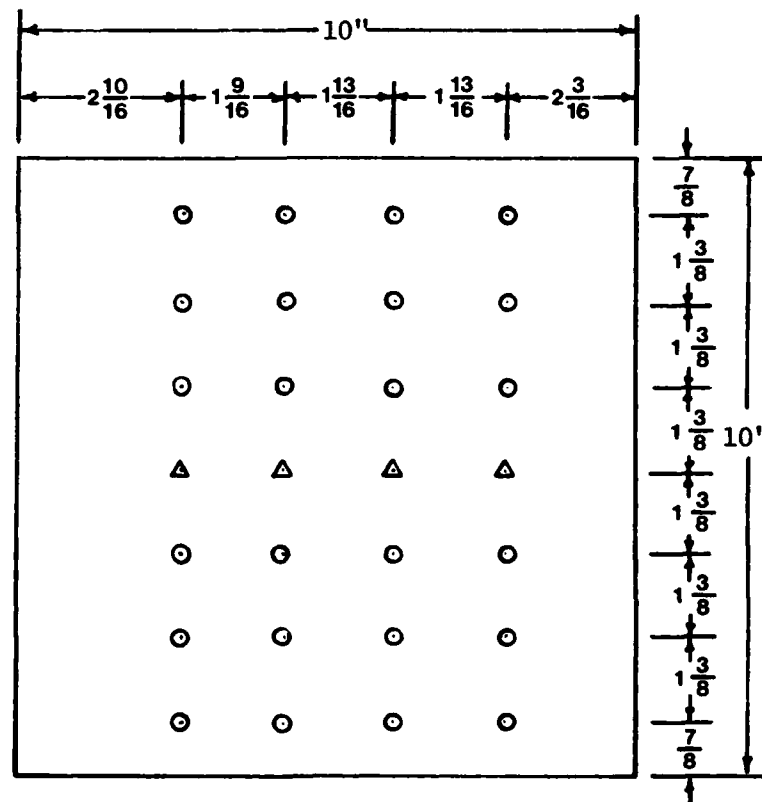


Fig. 11. Thermocouple System Wiring Diagram



- - Thermocouple Output: Strip Chart Recorder
- Δ - Thermocouple Output: Digital Millivolt Meter

Fig. 12. Front Surface Thermocouple Location

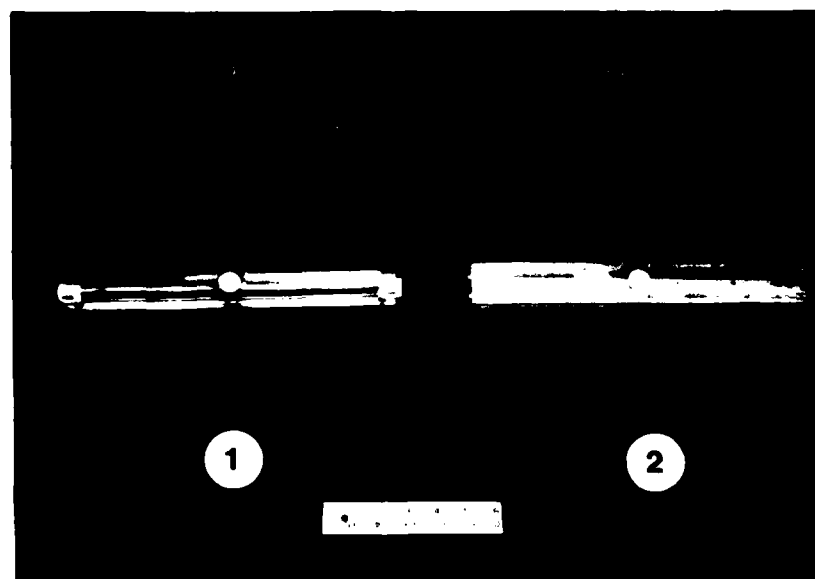


Fig. 13. View of Emitters: (1) Stretched Wire Emitter,
(2) Multipoint Emitter

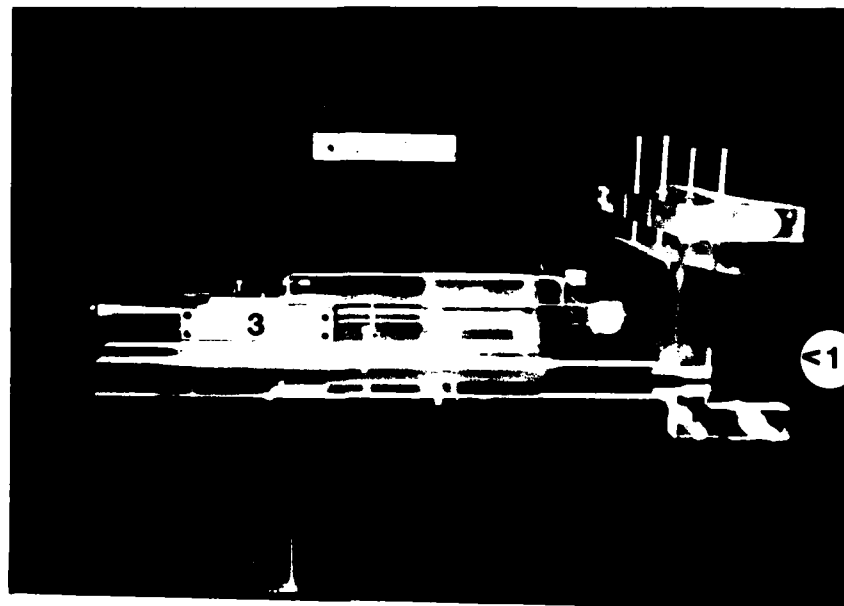


Fig. 14. View of Test Apparatus C: (1) Variable Nozzle with Grid Accelerator, (2) Stretched Wire Emitter Probe and (3) Micrometer Traversing Device

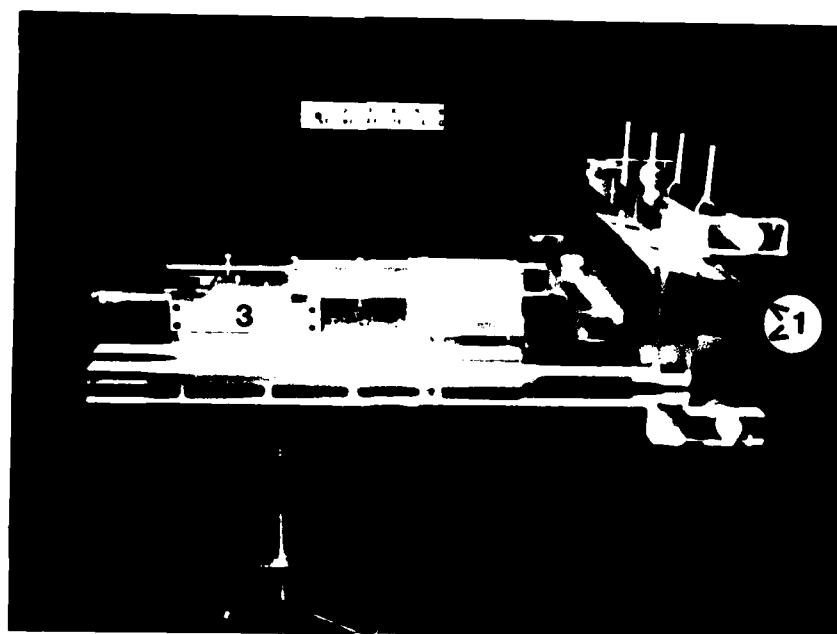


Fig. 15. View of Test Apparatus D: (1) Variable Nozzle, (2) Multipoint Emitter Probe and (3) Micrometer Traversing Device

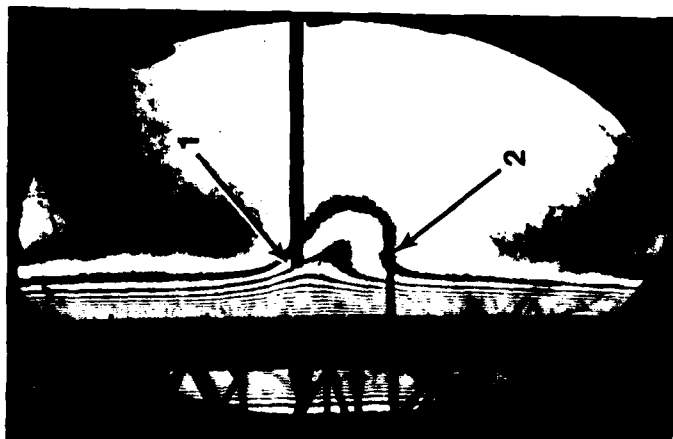


Photo 1

$P=0.012$ w
 $V=4.2$ kV
 $\zeta_e=0.5$ in.

Stretched Wire Emitter

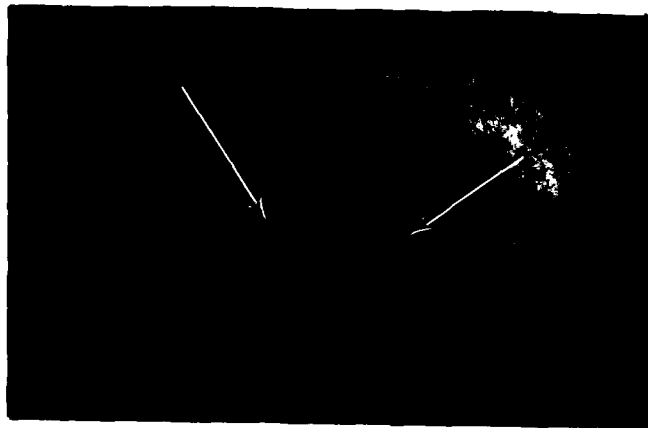


Photo 2

$P=0.025$ w
 $V=3.5$ kV
 $\zeta_e=0.5$ in.

Multipoint Emitter

Fig. 16. Interference Photographs Showing the Initial Effect of an Electric Field on the Thermal Boundary Layer of a Vertical Plate for a Stretched Wire and a Multipoint Emitter: (1) Stretched Wire Emitter, (2) Reference tee 2.0 in. and (3) Multipoint Emitter

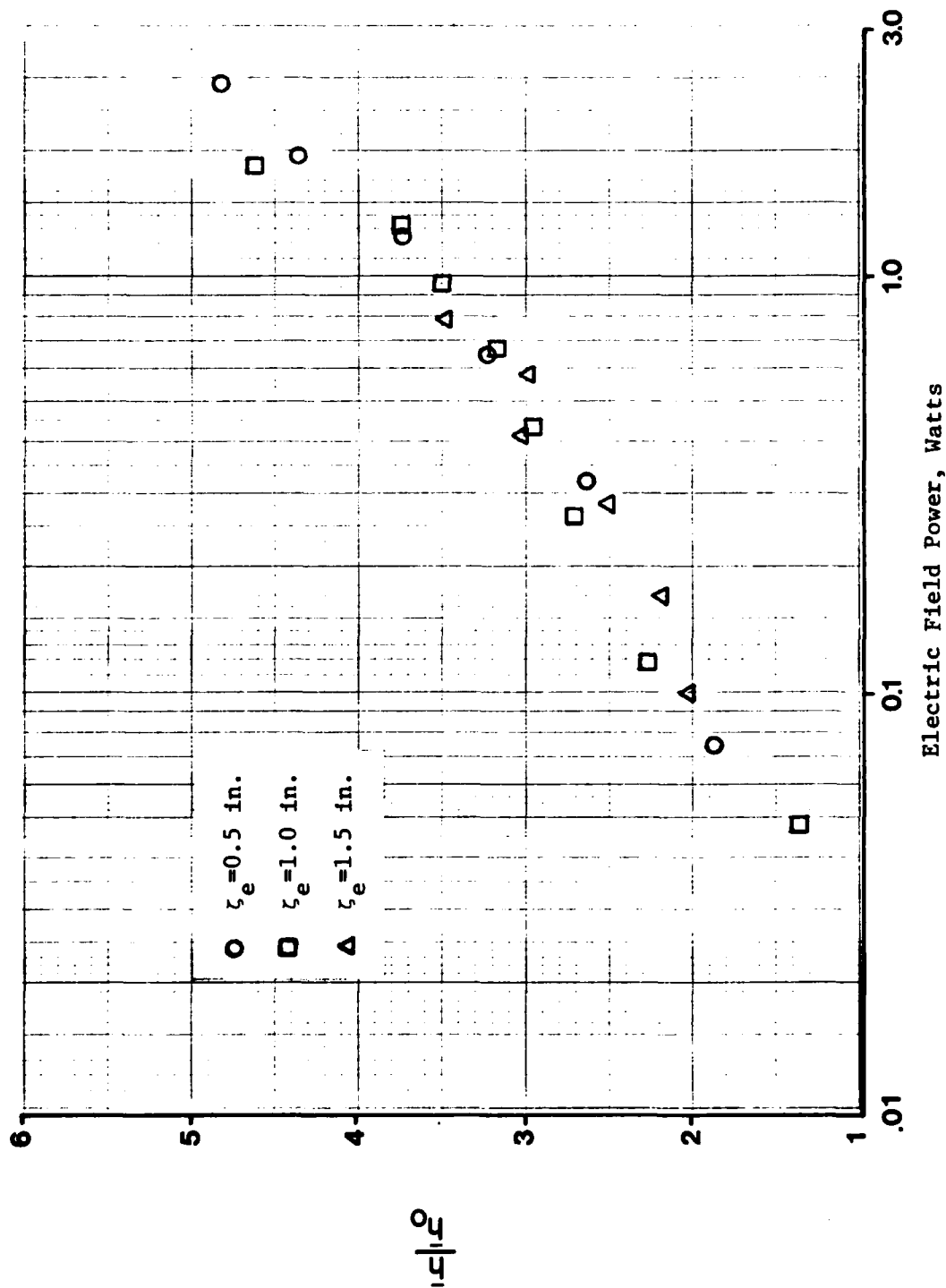


Fig. 17. Effect of Electric Field on the Ratio \bar{h}/\bar{h}_0 for the Stretched Wire Emitter at Various Plate-to-Emitter Distances z_e

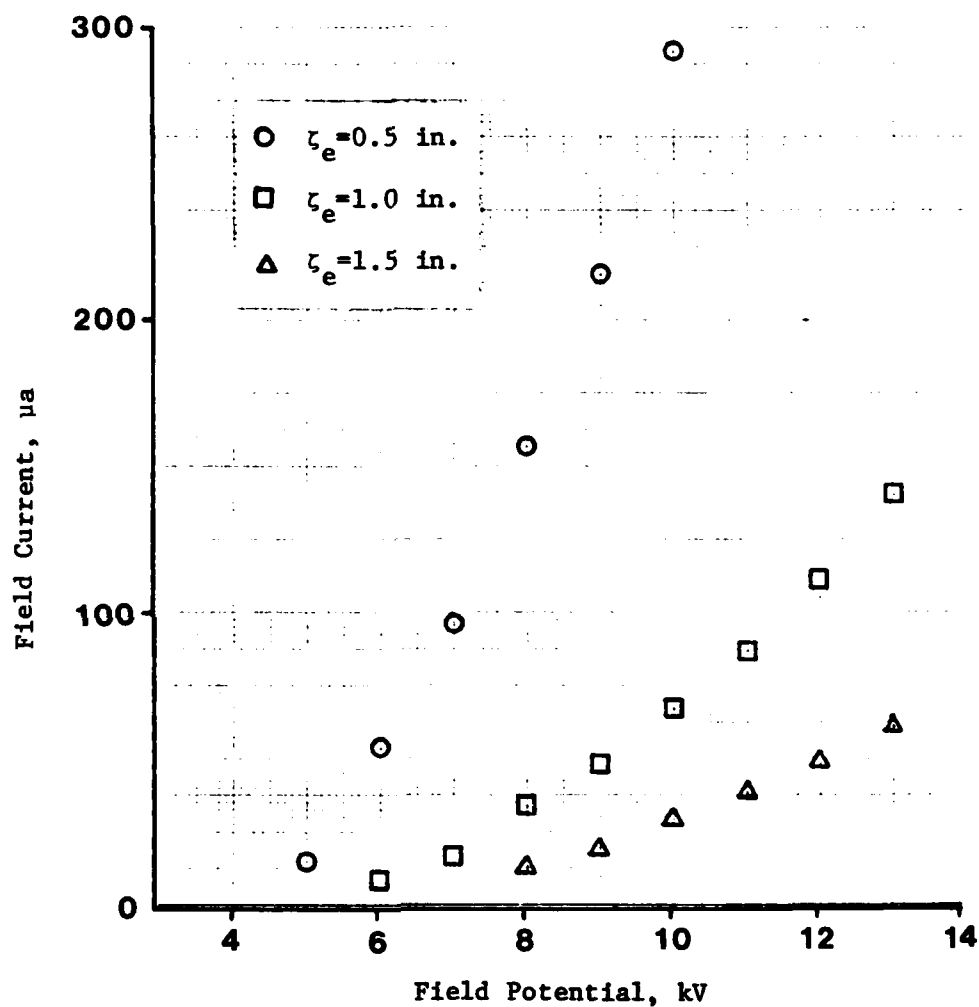


Fig. 18. Current, Voltage Relationship for the Stretched Wire Emitter at Various Plate-to-Emitter Distances ζ_e

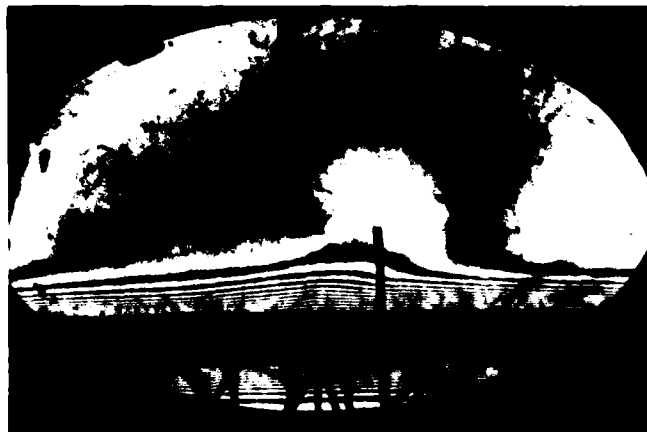


Photo 1

$P=0.007$ w
 $V=5.0$ kV
 $\zeta_e=1.0$ in.

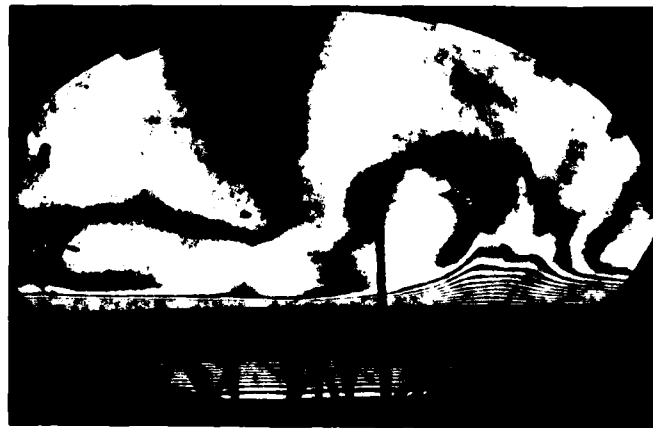


Photo 2

$P=0.048$ w
 $V=6.0$ kV
 $\zeta_e=1.0$ in.



Photo 3

$P=0.264$ w
 $V=8.0$ kV
 $\zeta_e=1.0$ in.

Fig. 19. Interference Photographs Showing the Effects of an Electric Field on the Thermal Boundary Layer of a Vertical Plate Using the Stretched Wire Emitter at Constant Plate-to-Emitter Distance ($\zeta_e=1.0$ in.)



Photo 4

$P=0.670$ w
 $V=10.0$ kV
 $\zeta_e=1.0$ in.

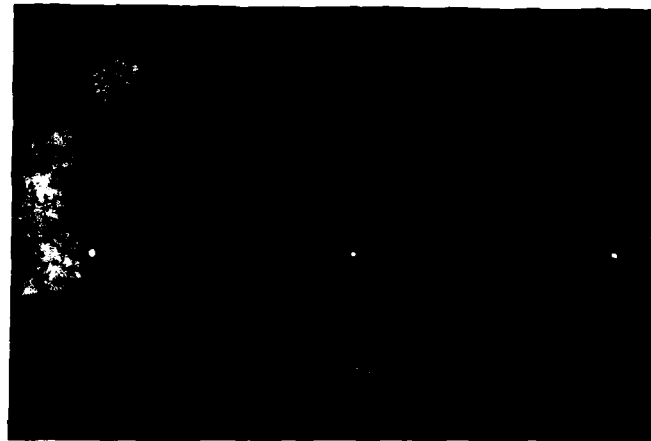


Photo 5

$P=1.332$ w
 $V=12.0$ kV
 $\zeta_e=1.0$ in.

Fig. 19 (Contd.). Interference Photographs Showing the Effects of an Electric Field on the Thermal Boundary Layer of a Vertical Plate Using the Stretched Wire Emitter at Constant Plate-to-Emitter Distance ($\zeta_e=1.0$ in.)

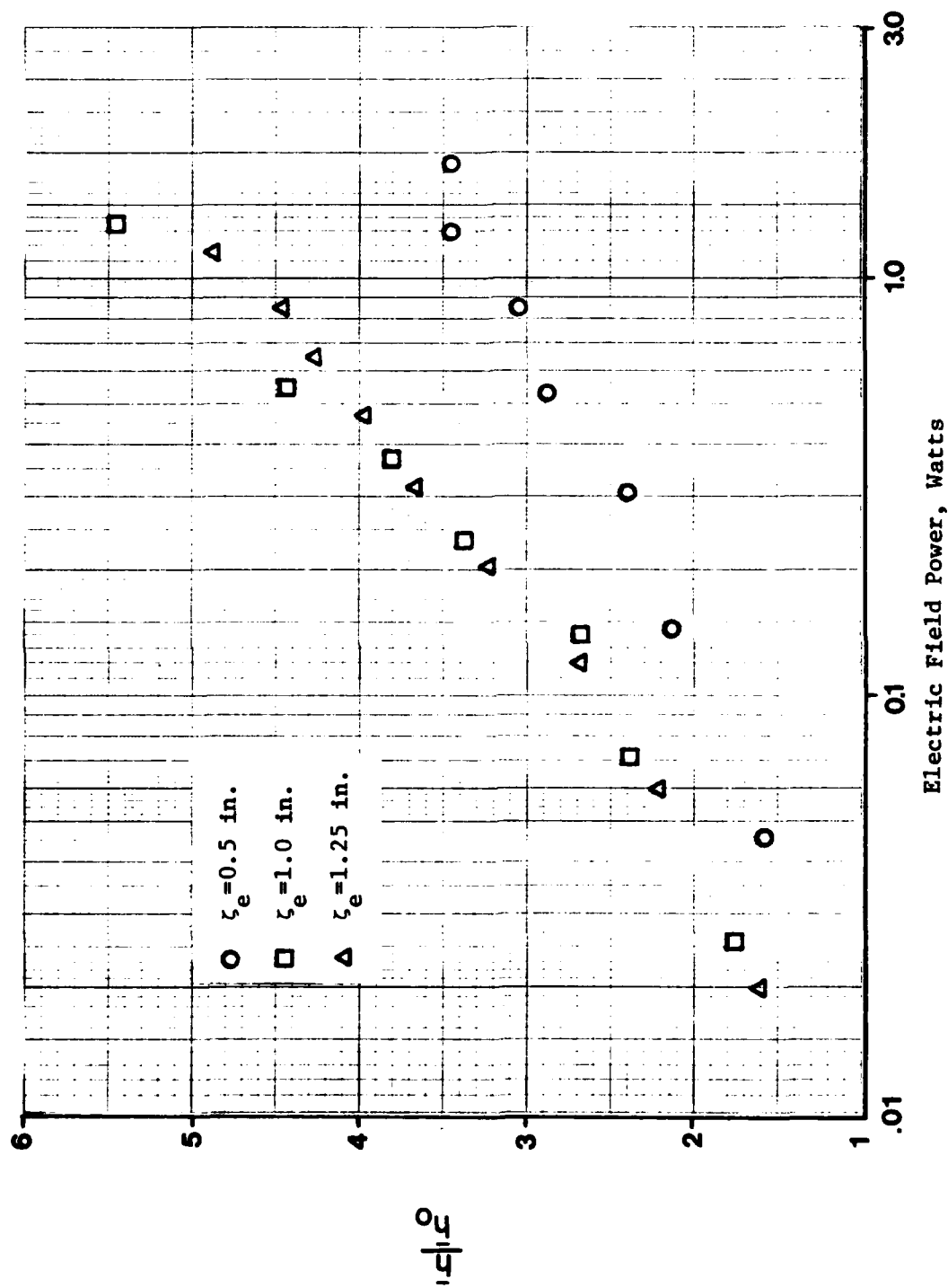


Fig. 20. Effect of Electric Field on the Ratio \bar{h}/\bar{h}_0 for the Multipoint Emitter at Various Plate-to-Emitter Distances z_e

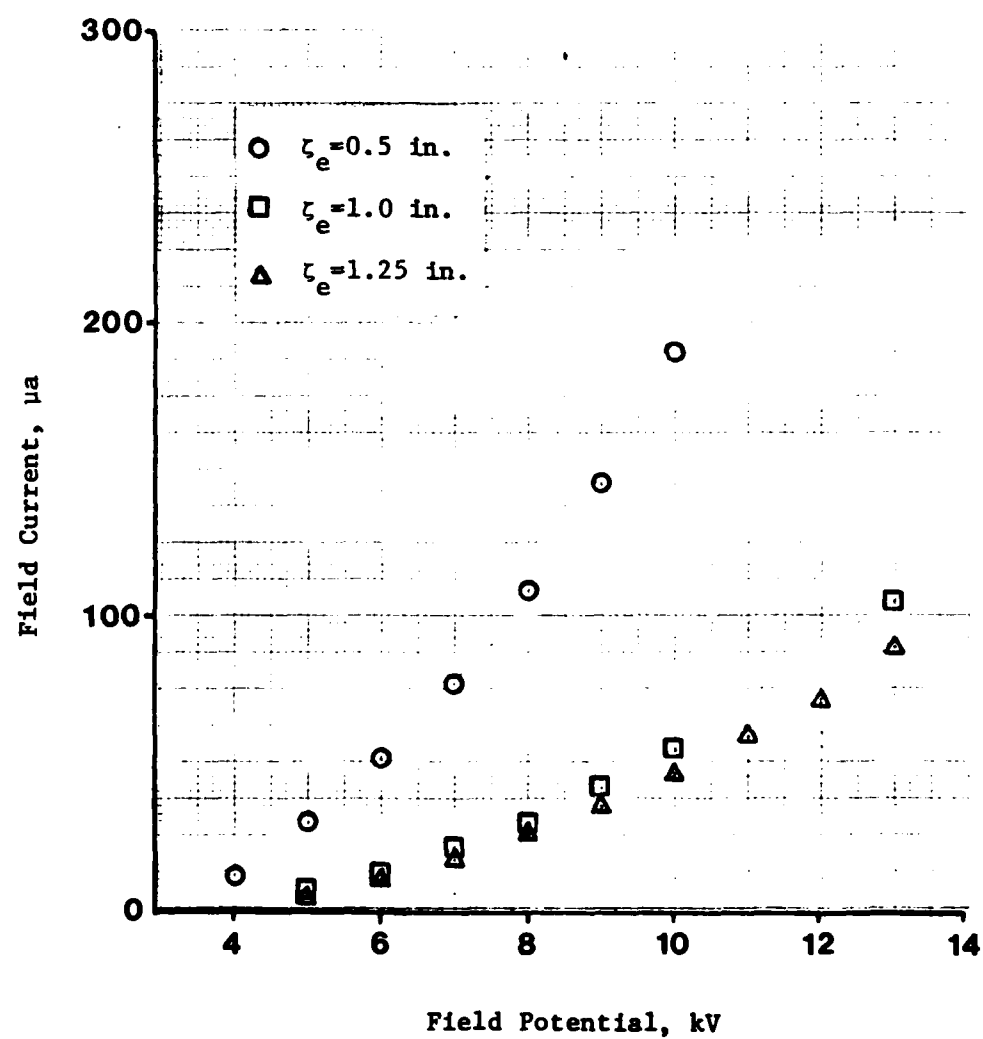


Fig. 21. Current, Voltage Relationship for the Multipoint Emitter at Various Plate-to-Emitter Distances ζ_e

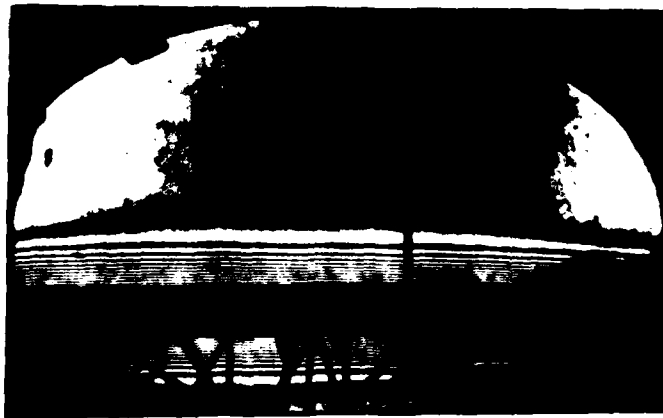


Photo 1

$P=0.0$ w
 $V=0.0$ kV
 $\zeta_e=1.0$ in.

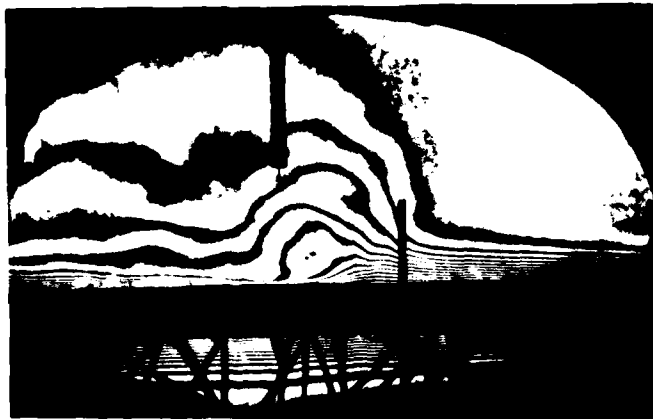


Photo 2

$P=0.026$ w
 $V=5.0$ kV
 $\zeta_e=0.0$ in.



Photo 3

$P=0.071$ w
 $V=6.0$ kV
 $\zeta_e=1.0$ in.

Fig. 22. Interference Photographs Showing the Effects of an Electric Field on the Thermal Boundary Layer of a Vertical Plate Using the Multipoint Emitter at Constant Plate-to-Emitter Distance ($\zeta_e=1.0$ in.)



Photo 4

$P=0.237$ w
 $V=8.0$ kV
 $z_e=1.0$ in.



Photo 5

$P=0.545$ w
 $V=10.0$ kV
 $z_e=1.0$ in.

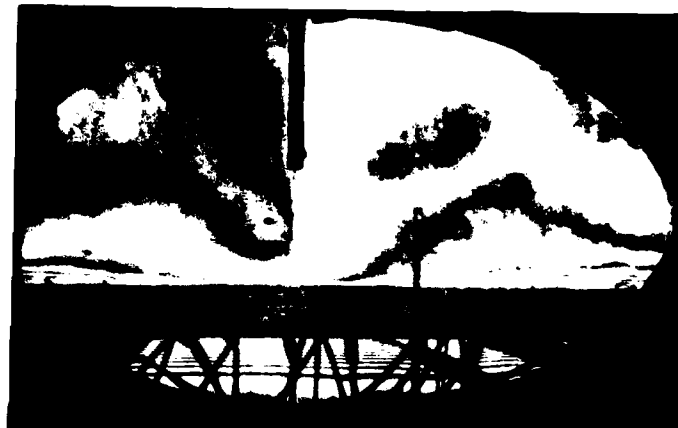


Photo 6

$P=1.044$ w
 $V=12.0$ kV
 $z_e=1.0$ in.

Fig. 22 (Contd.). Interference Photographs Showing the Effects of an Electric Field on the Thermal Boundary Layer of a Vertical Plate Using the Multipoint Emitter at Constant Plate-to-Plate Distance ($z_e=1.0$ in.)

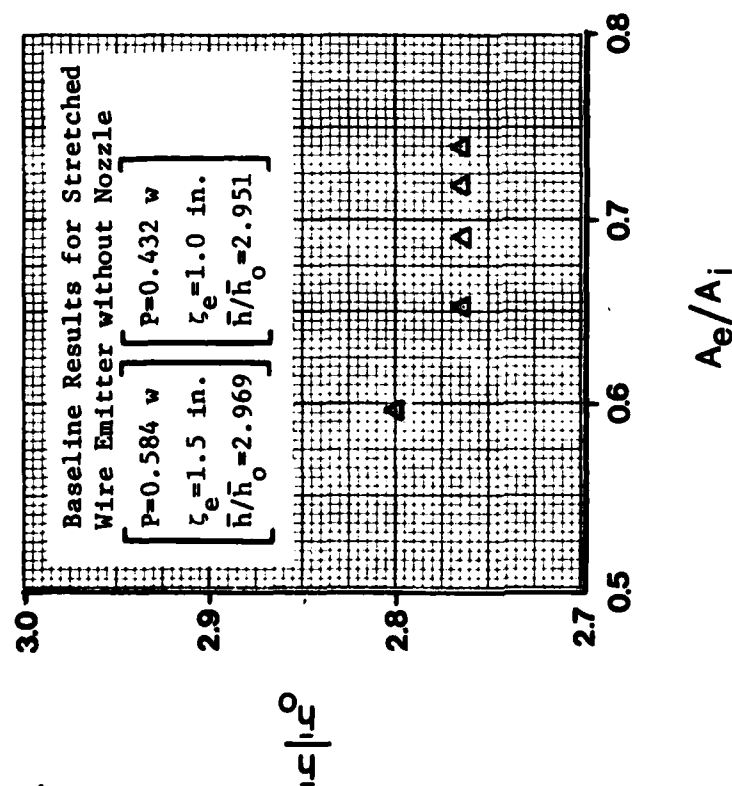


Fig. 23. Effect of Nozzle Area Ratio A_e/A_i on the Ratio \bar{h}/\bar{h}_0 for the Stretched Wire Emitter and Grid Accelerator. Field Power Maintained at 0.545 w, ($\zeta_n = 1.0 \text{ in.}$)

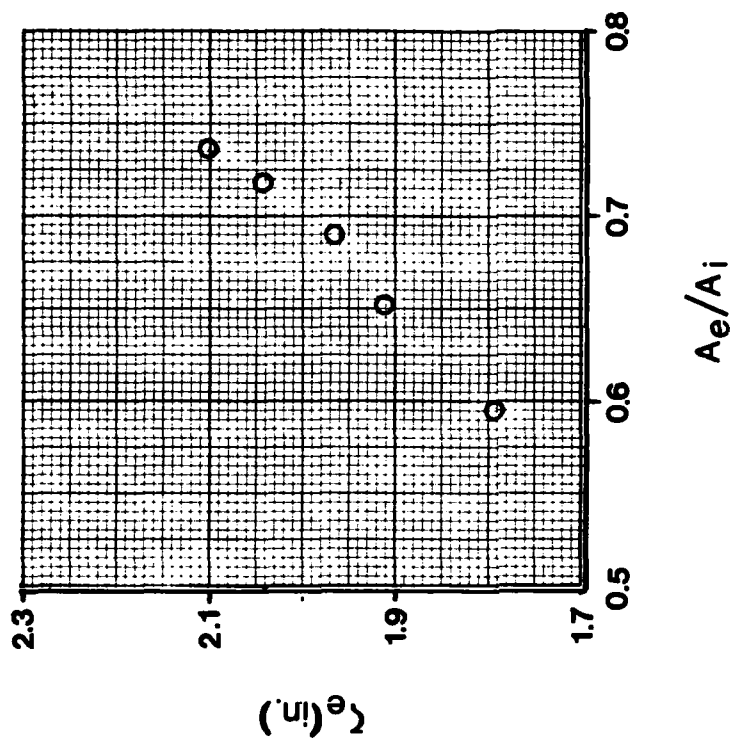


Fig. 24. Plate-to-Emitter Distance z_e Required to Maintain Constant Field Power ($P=0.545 \text{ w}$) for Various Nozzle Area Ratios A_e/A_i Using the Stretched Wire Emitter and Grid Accelerator



Photo 1

$P=0.545$ w
 $V=10.0$ kV
 $A_e/A_i=0.596$
 $\zeta_e=1.79$ in.
 $\zeta_n=1.0$ in.



Photo 2

$P=0.545$ w
 $V=10.0$ kV
 $A_e/A_i=0.651$
 $\zeta_e=1.91$ in.
 $\zeta_n=1.0$ in.

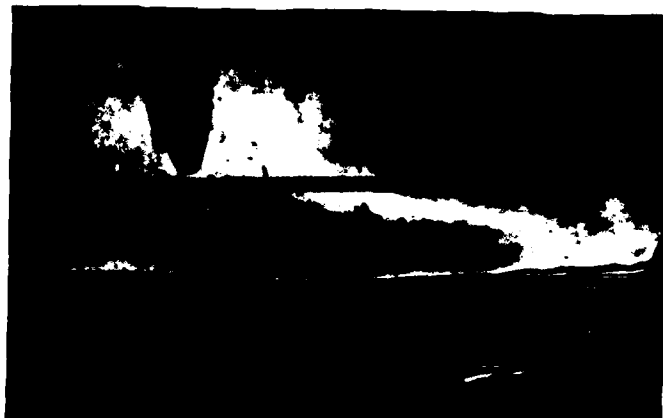


Photo 3

$P=0.545$ w
 $V=10.0$ kV
 $A_e/A_i=0.689$
 $\zeta_e=1.97$ in.
 $\zeta_n=1.0$ in.

Fig. 25. Interference Photographs Showing the Effects of an Electric Field on the Thermal Boundary Layer of a Vertical Plate with Various Nozzle Area Ratios A_e/A_i and Grounded Grid Acceleration ($\zeta_n=1.0$ in.) Using the Stretched Wire Emitter. Plate-to-Emitter Distance ζ_e Varied to Maintain Constant Field Power P



Photo 4

$P=0.545$ w
 $V=10.0$ kV
 $A_e/A_i=0.718$
 $\zeta_e=2.04$ in.
 $\zeta_n=1.0$ in.

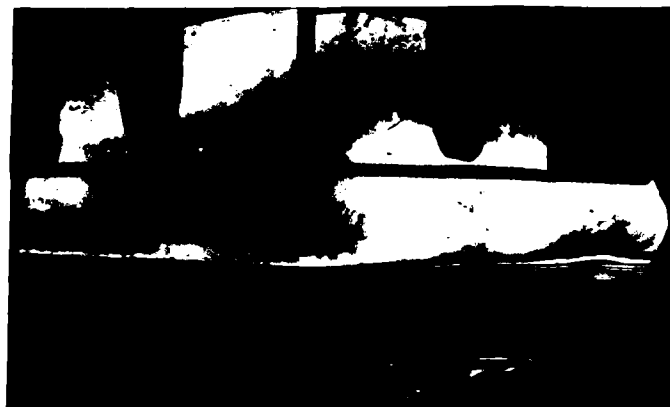


Photo 5

$P=0.545$ w
 $V=10.0$ kV
 $A_e/A_i=0.736$
 $\zeta_e=2.10$ in.
 $\zeta_n=1.0$ in.

Fig. 25 (Contd.). Interference Photographs Showing the Effects of an Electric Field on the Thermal Boundary Layer of a Vertical Plate with Various Nozzle Area Ratios A_e/A_i and Grounded Grid Acceleration ($\zeta_n=1.0$ in.) Using the Stretched Wire Emitter. Plate-to-Emitter Distance ζ_e Varied to Maintain Constant Field Power P .

\square_1 $P=0.552$ w	\square_4 $P=0.569$ w
\square_2 $P=0.554$ w	\square_5 $P=0.566$ w
\square_3 $P=0.568$ w	\square_6 $P=0.568$ w

$\bar{h}^*/\bar{h}_0 = 4.44$, multipoint emitter without
nozzle, $P=0.545$ w, $\zeta_e=1.0$ in.

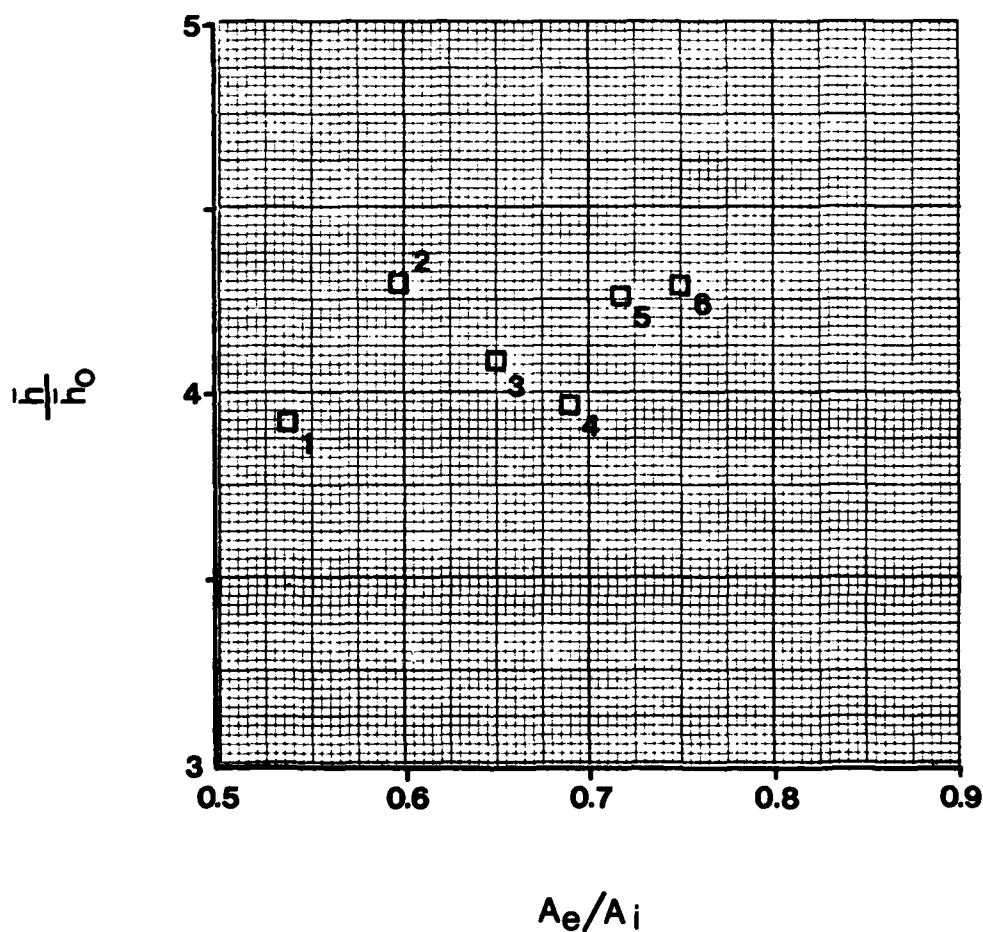


Fig. 26. Effect of Varying Nozzle Area Ratio A_e/A_i on the Ratio \bar{h}^*/\bar{h}_0 with the Multipoint Emitter. Plate-to-Emitter Distance ζ_e and Plate-to-Nozzle Distance ζ_n Fixed at 1.0 in.



Photo 1

$P=0.552$ w
 $V=10.5$ kV
 $A_e/A_i=0.537$
 $\zeta_n=1.0$ in.
 $\zeta_e=1.0$ in.



Photo 2

$P=0.554$ w
 $V=9.9$ kV
 $A_e/A_i=0.596$
 $\zeta_n=1.0$ in.
 $\zeta_e=1.0$ in.



Photo 3

$P=0.568$ w
 $V=9.8$ kV
 $A_e/A_i=0.651$
 $\zeta_n=1.0$ in.
 $\zeta_e=1.0$ in.

Fig. 27. Interference Photographs Showing the Effects of an Electric Field on the Thermal Boundary Layer of a Vertical Plate with Various Nozzle Area Ratios A_e/A_i Using the Multipoint Emitter



Photo 4

$P=0.569$ w
 $V=9.75$ kV
 $A_e/A_i=0.689$
 $\zeta_n=1.0$ in.
 $\zeta_e=1.0$ in.

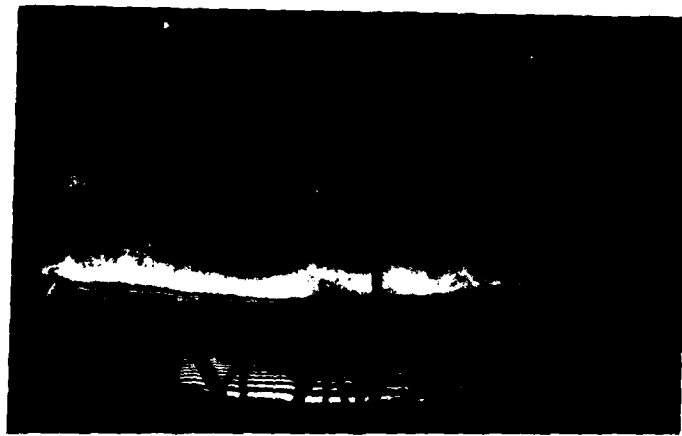


Photo 5

$P=0.566$ w
 $V=9.75$ kV
 $A_e/A_i=0.718$
 $\zeta_n=1.0$ in.
 $\zeta_e=1.0$ in.



Photo 6

$P=0.568$ w
 $V=9.7$ kV
 $A_e/A_i=0.750$
 $\zeta_n=1.0$ in.
 $\zeta_e=1.0$ in.

Fig. 27 (Contd.). Interference Photographs Showing the Effects of an Electric Field on the Thermal Boundary Layer of a Vertical Plate with Various Nozzle Area Ratios A_e/A_i Using the Multipoint Emitter

$\bar{h}^*/\bar{h}_0 = 4.44$, multipoint emitter without
nozzle, $P=0.545$ w, $\zeta_e=1.0$ in.

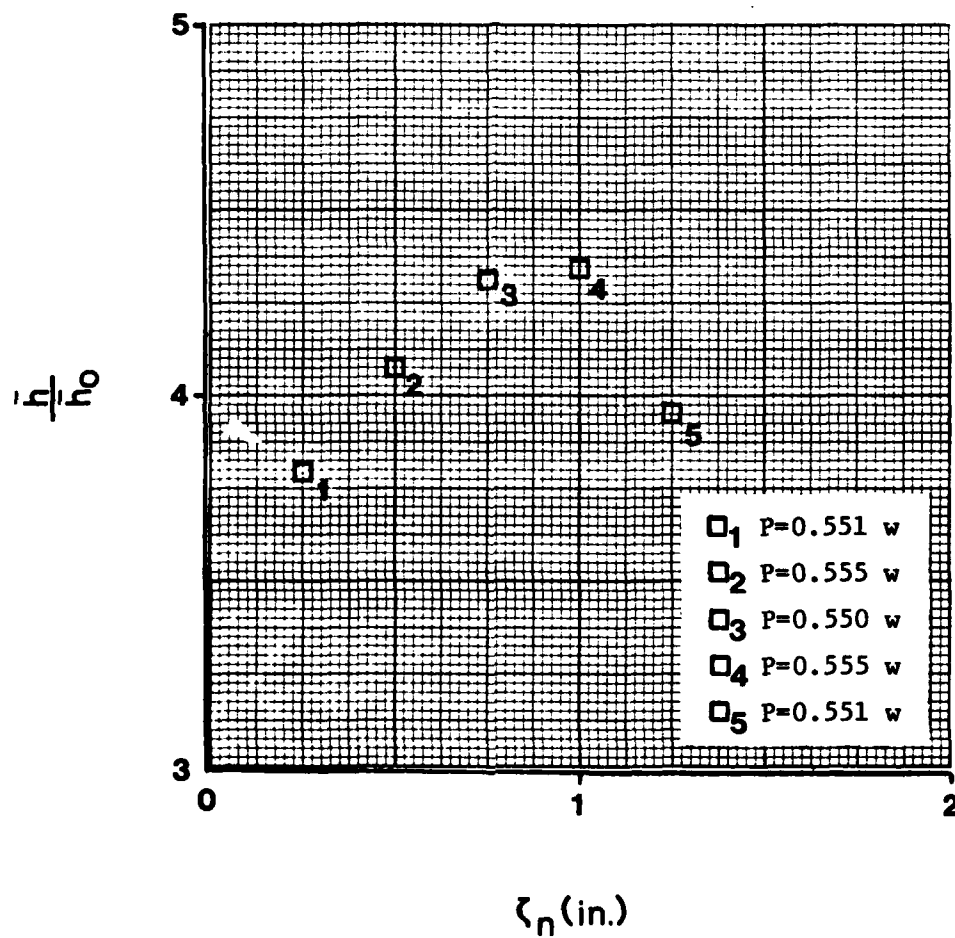


Fig. 28. Effect of Varying Plate-to-Nozzle Distance ζ_n on the Ratio h/\bar{h}_0 with the Multipoint Emitter Fixed at $\zeta_e=1.0$ in. and the Nozzle Area Ratio Fixed at $A_e/A_1=0.596$



Photo 1

$P=0.551$ w
 $V=12.2$ kV
 $A_e/A_i=0.596$
 $\zeta_n=0.25$ in.
 $\zeta_e=1.0$ in.



Photo 2

$P=0.555$ w
 $V=11.8$ kV
 $A_e/A_i=0.596$
 $\zeta_n=0.50$ in.
 $\zeta_e=1.0$ in.



Photo 3

$P=0.550$ w
 $V=11.0$ kV
 $A_e/A_i=0.596$
 $\zeta_n=0.75$ in.
 $\zeta_e=1.0$ in.

Fig. 29. Interference Photographs Showing the Effects of an Electric Field on the Thermal Boundary Layer of a Vertical Plate for Various Nozzle-to-Plate Distances ζ_n with Nozzle Area Ratio Constant ($A_e/A_i=0.596$) Using the Multipoint Emitter ($\zeta_e=1.0$ in.)



Photo 4

$P=0.555$ w
 $V=10.2$ kV
 $A_e/A_i=0.596$
 $\zeta_n=1.0$ in.



Photo 5

$P=0.551$ w
 $V=10.0$ kV
 $A_e/A_i=0.596$
 $\zeta_n=1.25$ in.

Fig. 29 (Contd.). Interference Photographs Showing the Effects of an Electric Field on the Thermal Boundary Layer of a Vertical Plate for Various Nozzle-to-Plate Distances ζ_n with Nozzle Area Ratio Constant ($A_e/A_i=0.596$) Using the Multipoint Emitter ($\zeta_e=1.0$ in.)

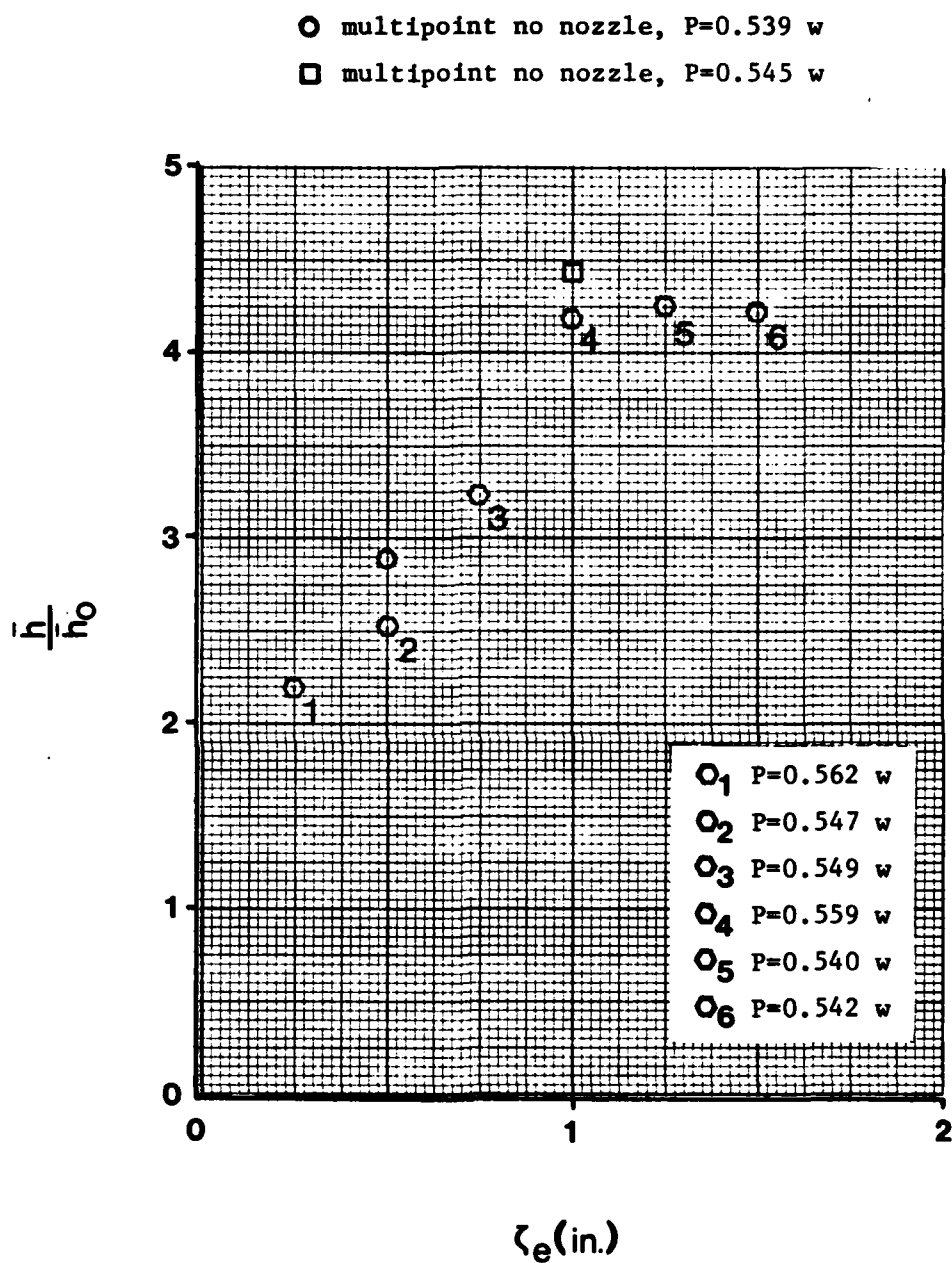


Fig. 30. Effect of Varying Plate-to-Emitter Distance ζ_e on the Ratio $\frac{h}{h_0}$ for the Multipoint Emitter with Nozzle. Nozzle Area Ratio $A_e/A_1=0.596$ Fixed and Plate-to-Nozzle Distance ($\zeta_n=1.0$ in.) Fixed



Photo 1

$P=0.562 \text{ w}$
 $V=5.2 \text{ kv}$
 $A_e/A_i=0.596$
 $\zeta_n=1.0 \text{ in.}$
 $\zeta_e=0.25 \text{ in.}$



Photo 2

$P=0.547 \text{ w}$
 $V=7.2 \text{ kv}$
 $A_e/A_i=0.596$
 $\zeta_n=1.0 \text{ in.}$
 $\zeta_e=0.50 \text{ in.}$



Photo 3

$P=0.549 \text{ w}$
 $V=8.65 \text{ kv}$
 $A_e/A_i=0.596$
 $\zeta_n=1.0 \text{ in.}$
 $\zeta_e=0.75 \text{ in.}$

Fig. 31. Interference Photographs Showing the Effects of an Electric Field on the Thermal Boundary Layer of a Vertical Plate at Various Plate-to-Emitter Distances ζ_e Using the Multipoint Emitter. Nozzle Area Ratio ($A_e/A_i=0.596$) and Plate-to-Nozzle Distance ($\zeta_n=1.0 \text{ in.}$) Maintained Constant



Photo 4

$P=0.559 \text{ w}$
 $V=10.2 \text{ kV}$
 $A_e/A_i=0.596$
 $\zeta_n=1.0 \text{ in.}$
 $\zeta_e=1.0 \text{ in.}$



Photo 5

$P=0.540 \text{ w}$
 $V=11.4 \text{ kV}$
 $A_e/A_i=0.596$
 $\zeta_n=1.0 \text{ in.}$
 $\zeta_e=1.25 \text{ in.}$



Photo 6

$P=0.542 \text{ w}$
 $V=14.0 \text{ kV}$
 $A_e/A_i=0.596$
 $\zeta_n=1.0 \text{ in.}$
 $\zeta_e=1.5 \text{ in.}$

Fig. 31 (Contd.). Interference Photographs Showing the Effects of an Electric Field on the Thermal Boundary Layer of a Vertical Plate at Various Plate-to-Emitter Distances ζ_e Using the Multipoint Emitter. Nozzle Area Ratio ($A_e/A_i=0.596$) and Plate-to-Nozzle Distance ($\zeta_n=1.0 \text{ in.}$) Maintained Constant

Appendix I

Typical Properties of Test Plate Material

Military specification 2024 aluminum is a high strength aluminum alloy whose specifications described by ARDC-TR 59-66 are as follows:

Melting Range	935 to 1180 F
Emissivity in Air	0.035 to 0.070
Density	0.100 gm/cm ³
Electrical Resistivity	2.26 microhm in.
Magnetic Properties	nonmagnetic

Appendix II

Typical Properties of Thermocouple Epoxy, "Omegabond 101"

"Omegabond 101" is described by the manufacturer, Omega Engineering, Inc., as a versatile room-temperature cure, high thermal conductivity two-part epoxy designed specifically to permanently bond beaded wire thermocouples to a wide variety of materials.

The following properties of "Omegabond 101" are specified by the manufacturer (13):

Tensile Shear, 1/2" (1.27 cm) overlap	2,200 psi
Flexural Strength	12,000 psi
Coefficient of Thermal Expansion	20×10^{-6} in/in/F
Thermal Conductivity	7.2 BTU w/hr ft ² F
Thermal Conductivity	0.0025 cal cm/sec cm ³ C
Volume Resistivity	10^{15} ohm cm
Chemical and Solvent Resistance	Excellent
Color	White
Maximum Continuous Temperature	275 F (135 C)

Appendix III

VAX 11/780 Digital Computer Program

O'Brien's (4) digital computer program was used with minor revision to compute the heat transfer coefficients and wall temperatures along the plate. The program as revised is listed in Figure 32. Typical input and output data files are presented in Figures 33 and 34 respectively.

```

* STEFKOVICH GAE-83D INTERFEROMETER DATA REDUCTION
* L= RUN NUMBER
* XINCH= ACTUAL LENGTH OF REFERENCE WIRE, IN.
* XSCAL= MEASURED LENGTH OF PHOTOGRAPHED REFERENCE WIRE, IN.
* CM= MOLECULAR WEIGHT OF AIR, LBM/LB MOLE.
* NN= TOTAL NUMBER OF STATIONS BEING MEASURED
* KK= TOTAL NUMBER OF FRINGES
* TC= CHAMBER TEMPERATURE, R
* PC= CHAMBER PRESSURE, IN. OF HG.
REAL SD1(20),SD2(20),SD3(20),X1(20),X2(20),X3(20),H(20)
REAL TW(20),R(20),T(20)
REAL WALL(20),F1(20),F2(20),F3(20)
INTEGER L,NN,KK
REAL XINCH,XSCAL,CM,TC,PC
OPEN (UNIT=11,FILE='data')
OPEN (UNIT=12,FILE='output')
REWIND 11
REWIND 12
1 READ (11,10) L,XINCH,XSCAL,CM,NN,KK,TC,PC
10 FORMAT (12,2X,F3.1,2X,F6.4,2X,F5.2,2X,12,2X,12,2X,F5.1,2X,F6.3)
C=XINCH/XSCAL
S=KK
A=(70.73*CM*PC)/1545.4
RC=A/TC
DO 2 I=1,NN
20 READ (11,20) WALL(I),F1(I),F2(I),F3(I)
FORMAT (F6.4,2X,F6.4,2X,F6.4,2X,F6.4)
SD1(I)=ABS((F1(I)-WALL(I))*3937000)
SD2(I)=ABS((F2(I)-WALL(I))*3937000)
SD3(I)=ABS((F3(I)-WALL(I))*3937000)
X1(I)=C*SD1(I)
X2(I)=C*SD2(I)
2 X3(I)=C*SD3(I)
R(KK-2)=RC-(.000589*(S-2.5))
R(KK-1)=RC-(.000589*(S-1.5))
R(KK)=RC-(.000589*(S-.5))
T(KK-2)=A/R(KK-2)
T(KK-1)=A/R(KK-1)
T(KK)=A/R(KK)
DELT1=T(KK)-T(KK-1)
DELT2=T(KK-1)-T(KK-2)
5 CK=.01516+(T(KK)-540.)*.00657/270.
DO 6 I=1,NN
GRAD1=DELT1/(X2(I)-X1(I))
GRAD2=DELT2/(X3(I)-X2(I))
AV=.5*(GRAD1+GRAD2)
TW(I)=T(KK)+AV*X1(I)
H(I)=(12.*CK*AV)/(TW(I)-TC)
103 WRITE (12,103) I,TW(I),H(I)
FORMAT (/10X,'I=',I3,5X,'TW=',F13.8,8X,'H=',F10.8)
104 WRITE (12,104) GRAD1,GRAD2
104 FORMAT (/20X,'GRAD1=',F13.8,5X,'GRAD2=',F13.8)
IF (I-1) 7,7,6
7 WRITE (12,105) T(KK),T(KK-1),T(KK-2)
105 FORMAT (/20X,'TF1=',F6.2,2X,'TF2=',F6.2,2X,'TF3=',F6.2)
6 CONTINUE
END

```

Fig. 32. Source Program Used with the VAX 11/780 Computer

01	2.0	1.0490	28.95	13	10	537.0	29.03
2.7700	2.7890	2.8250	2.8670				
2.7740	2.7950	2.8360	2.8760				
2.7730	2.8000	2.8400	2.8750				
2.7720	2.7990	2.8380	2.8760				
2.7730	2.7970	2.8340	2.8690				
2.7610	2.7830	2.8200	2.8570				
3.0710	3.0940	3.1330	3.1660				
3.0750	3.0950	3.1300	3.1650				
3.0700	3.0910	3.1240	3.1550				
3.0610	3.0810	3.1100	3.1410				
3.0510	3.0690	3.0950	3.1260				
3.0540	3.0730	3.1010	3.1280				
3.0340	3.0510	3.0690	3.0940				

Fig. 33. Typical Input Data File

I= 1	TW= 587.59130859	H= .71536988
	GRAD1= 201.54515076	GRAD2= 169.56610107
	TF1=584.94 TF2=579.50	TF3=574.15
I= 2	TW= 587.74298096	H= .68229049
	GRAD1= 176.96702576	GRAD2= 178.04484558
I= 3	TW= 588.84497070	H= .72395217
	GRAD1= 181.39088440	GRAD2= 203.47914124
I= 4	TW= 588.72930908	H= .70405591
	GRAD1= 186.04156494	GRAD2= 187.41610718
I= 5	TW= 588.54412842	H= .75600445
	GRAD1= 196.09712219	GRAD2= 203.48048401
I= 6	TW= 588.15338135	H= .74080938
	GRAD1= 196.09837341	GRAD2= 192.47978210
I= 7	TW= 588.41381836	H= .76223946
	GRAD1= 186.04272461	GRAD2= 215.81179810
I= 8	TW= 588.02838135	H= .78506166
	GRAD1= 207.30313110	GRAD2= 203.48048401
I= 9	TW= 588.48852539	H= .85157233
	GRAD1= 219.86758423	GRAD2= 229.73577881
I= 10	TW= 588.54742432	H= .90797353
	GRAD1= 250.19570923	GRAD2= 229.73408508
I= 11	TW= 588.38214111	H= .96568573
	GRAD1= 279.06237793	GRAD2= 229.73582458
I= 12	TW= 588.67370605	H= .98684853
	GRAD1= 269.12847900	GRAD2= 263.77038574
I= 13	TW= 589.33441162	H= 1.28197753
	GRAD1= 403.09298706	GRAD2= 284.87036133

Fig. 34. Typical Output Data File

Appendix IV

Equipment List and Specifications

Equipment used during the experimental portion of the study is listed in the following manner: name, manufacturer, model number (MD) or type number (TN), serial number (SN), and range.

Interferometer and Camera System

1. Interferometer, Gaertner Scientific Corp., 8 in. optics.
2. Light Source (interferometer), General Electric Co., Magda sun-light lamp, TN S-4, 100 watt.
3. Mirror (concave), focal length 45 in., 7.5 in. diameter.
4. Mirror (plane), 7.5 in. diameter.
5. Polaroid Camera Back, Graflex Inc., with Type 42 and 47 Polaroid film.

High Voltage System (DC)

1. High Voltage DC Power Supply, NJE Corp., T H-30-35, SN 11806, 0-30 kV, 0-35 ma.
2. Electrostatic Voltmeter, Sensitive Research Instrument Corp., MD ESH, SN 102132, 0-15 kV.
3. Microammeter, Hewlett-Packard Co., MD 3466A SN 1716A-15917, 0-200 ma and 0-2 ma.
4. Electric Field Wire (Nichrome Alloy), Driver-Harris Co., 0.002 in. diameter.
5. High Voltage Lead Wire, Beldon, TN 8866, 40 kV max.

Low Voltage System (AC)

1. Wattmeter, Weston Electric Instrument Corp., MD 310, SN 17964, 0-120 watts.

2. Ammeter (AC), Hewlett-Packard, MD 3466A, SN 1716A-18320, 0-2000 ma (RMS).
3. Voltmeter (AC), John Fluke Manufacturing Co., MD 8100B, ID49100/4H6654, 0-100 volts.
4. Main Variable Transformer, The Superior Electric Co., TN 2PF136, 0-140 volts, 20 a.
5. Variable Auto Transformer, Standard Electric Product Co., TN 500B, 0-135 volts, 7.5 a.
6. Heater Element Wire (Nichrome Alloy), Driver-Harris Co., 0.0125 in. diameter.

Thermocouple System

1. Thermocouple Wire, Honeywell, MD 9B1N4, 24 gage Copper-Constantan, nylon coated.
2. Strip Chart Recorder, Honeywell, MD Electronik 16, SN SR5760992002, 0-1 mV.
3. Thermocouple Sequencer, Omega Engineering Inc., MD Dataplex 10, SN 9270, 10 point.
4. Millivoltmeter, Hewlett-Packard, MD 3466A, SN 1716A-18299, 0-20 mV.
5. Dewar Flask (Ice Bath).

Miscellaneous Equipment

1. Traversing Microscope, Central Scientific Co., SN 78039-2279.
2. Thermometer, Fisher Scientific, MD 14-983-15B, 0-230 F.
3. Barometer, Henry J. Green Instruments, MD ML-512A/GM, SN 10.
4. Sling Psychrometer, Taylor Instrument Co.
5. Programmable DC Voltage/Current Generator, Soltec, MD 6141, SN 17580085.
6. Potentiometer, Honeywell, MN 2745, ID 49300/4H4335.

Bibliography

1. Robinson, M. "Movement of Air in the Electric Wind of the Corona Discharge," AIEE Transactions, 801: 143-150 (May 1961).
2. Velkoff, R. R. "Electrofluidmechanics: Investigation of the Effects of Electrostatic Fields on Heat Transfer and Boundary Layers," ASD-TDR 62-650, Aeronautical System Division, Air Force Systems Command, WPAFB, OH, 1962.
3. Velkoff, H. R. and Marco, S. M. "Effect of Electrostatic Fields on Free-Convection Heat Transfer from Flat Plates," ASME Paper 62-HT-9, ASME-AICHE Joint Meeting on Heat Transfer, Boston, Mass, Aug. 1963.
4. O'Brien, R. J. and Shine, A. J. "Some Effects of an Electric Field on Heat Transfer from a Vertical Plate in Free Convection," ASME Journal of Heat Transfer, 89: 114-116 (Feb. 1967).
5. Franke, M. E. "Effect of Vortices Induced by Corona Discharge on Free Convection Heat Transfer from a Vertical Plate," ASME Journal of Heat Transfer, 89: 427-433 (Aug. 1969).
6. Demorest, K. E. and Gause, R. L. "Parameters Affecting Electrostatic Cooling," Internal Note IN-EH 11-74-2, Engineering Physics Div., Materials and Processes Lab., NASA/Marshall Space Flight Center, MSFC, AL, 9 Sept. 1974.
7. Shannon, R. L. and Pogson, J. T. "Electronics Electrostatic Cooling," Final Report prepared for Naval Air Systems Command (AIR-52022), Washington D.C., April 1977 (AD-B020432).
8. Kennard, R. B. "An Optical Method for Measuring Temperature Distribution and Convective Heat Transfer," Bureau of Standards Journal of Research, 8: 787 (1932).
9. Shapiro, A. H. The Dynamics and Thermodynamics of Compressible Fluid Flow, Volume I, New York: John Wiley and Sons, Inc., 60-65, 1953.
10. O'Brien, R. J. The Effect of an Electric Field on Heat Transfer from a Vertical Plate in Various Gases over a Range of Pressures. MS thesis, GA/ME/64-3, School of Engineering, Air Force Institute of Technology (AU), WPAFB, OH, 44-49, Aug. 1964.
11. Schlichting, H. Boundary-Layer Theory (Seventh Edition). New York: McGraw-Hill Book Company, 315-320, 1979.

12. Franke, M. E. Effects of Electrostatic Fields on Free Convection Heat Transfer from Plates in Air. PhD dissertation. The Ohio State University, Columbus, OH, 17-20, 1967.
13. OB-101. Technical Bulletin and Instruction Sheet. Omega Engineering Inc., Stamford, Conn, undated.

VITA

Michael Edward Stefkovich was born [REDACTED]

PII Redacted

[REDACTED] the son of [REDACTED] After graduation from [REDACTED] in 1966, he enrolled at West Virginia University. He graduated with high honors December 1970 with the degree of Bachelor of Science in Mechanical Engineering. After graduation he was employed as a Service Engineer in the Fossil Fuels Branch of the Babcock and Wilcox Company. He joined the United States Air Force in 1971 and was commissioned through Officer Training School. He completed Undergraduate Pilot Training at Laughlin Air Force Base in March 1973. He served as a C-141A Aircraft Commander (1973-1977), a T-38A Instructor Pilot/Flight Commander (1977-1981) and a T-39A Instructor Pilot until entering the School of Engineering, Air Force Institute of Technology, in October 1982.

Permanent address: [REDACTED]
[REDACTED] [REDACTED]

PII Redacted

UNCLASSIFIED

SECURITY CLASSIFICATION OF THIS PAGE

REPORT DOCUMENTATION PAGE

1a. REPORT SECURITY CLASSIFICATION Unclassified			1b. RESTRICTIVE MARKINGS	
2a. SECURITY CLASSIFICATION AUTHORITY			3. DISTRIBUTION/AVAILABILITY OF REPORT Approved for public release; distribution unlimited	
2b. DECLASSIFICATION/DOWNGRADING SCHEDULE				
4. PERFORMING ORGANIZATION REPORT NUMBER(S) AFIT/GAE/AA/83D-22			5. MONITORING ORGANIZATION REPORT NUMBER(S)	
6a. NAME OF PERFORMING ORGANIZATION School of Engineering		6b. OFFICE SYMBOL (If applicable) AFIT/ENY		7a. NAME OF MONITORING ORGANIZATION
6c. ADDRESS (City, State and ZIP Code) Air Force Institute of Technology Wright-Patterson AFB OH 45433			7b. ADDRESS (City, State and ZIP Code)	
8a. NAME OF FUNDING/SPONSORING ORGANIZATION		8b. OFFICE SYMBOL (If applicable)		9. PROCUREMENT INSTRUMENT IDENTIFICATION NUMBER
8c. ADDRESS (City, State and ZIP Code)			10. SOURCE OF FUNDING NOS.	
11. TITLE (Include Security Classification) See Box 19			PROGRAM ELEMENT NO.	PROJECT NO.
			TASK NO.	WORK UNIT NO.
12. PERSONAL AUTHOR(S) Michael E. Stefkovich, B.S., Maj, USAF				
13a. TYPE OF REPORT MS Thesis		13b. TIME COVERED FROM _____ TO _____		14. DATE OF REPORT (Yr., Mo., Day) 1983 December
15. PAGE COUNT 83				
16. SUPPLEMENTARY NOTATION				
17. COSATI CODES			18. SUBJECT TERMS (Continue on reverse if necessary and identify by block number) Approved for public release: LAW AFR 130-17. <i>Lynn E. Wolaver</i> Lynn E. WOLAVER Dean for Research and Professional Development Air Force Institute of Technology (AIG) Wright-Patterson AFB OH 45433 7 May 84	
FIELD	GROUP	SUB. GR.		
20	13			
19. ABSTRACT (Continue on reverse if necessary and identify by block number) Title: EFFECTS OF NOZZLE AND GRID ACCELERATION OF CORONA WIND ON COOLING OF A VERTICAL FLAT PLATE Thesis Chairman: Milton E. Franke, PhD Several experiments were conducted to determine the effect of nozzle and grid acceleration of a corona wind on the free convection heat transfer rate of a vertically mounted heated flat plate. The plate was maintained at ground potential and was suspended in a Mach-Zehnder interferometer. A positively charged stretched wire emitter and nineteen point emitter were used. Baseline tests were conducted to determine the changes in plate convective heat transfer rate attainable at various field power settings, and plate-to-emitter distances.				
20. DISTRIBUTION/AVAILABILITY OF ABSTRACT UNCLASSIFIED/UNLIMITED <input checked="" type="checkbox"/> SAME AS RPT. <input type="checkbox"/> DTIC USERS <input type="checkbox"/>			21. ABSTRACT SECURITY CLASSIFICATION Unclassified	
22a. NAME OF RESPONSIBLE INDIVIDUAL Milton E. Franke, PhD			22b. TELEPHONE NUMBER (Include Area Code) 513-255-2362	22c. OFFICE SYMBOL AFIT/ENY

DD FORM 1473, 83 APR

EDITION OF 1 JAN 73 IS OBSOLETE.

UNCLASSIFIED

SECURITY CLASSIFICATION OF THIS PAGE

Block 19 continued:

A two dimensional variable area convergent nozzle constructed of wood and plexiglas was used to accelerate the flow of the corona wind toward the plate. Nozzle inlet/exit area, plate-to-nozzle distance and plate-to-emitter distance was varied. A grid accelerator composed of an aluminum screen mesh was attached across the exit area of the convergent nozzle and was maintained at ground potential.

Plate heat transfer rates were determined from energy balance measurements and interferometer photographs. Results indicated that the nozzle and gride accelerator coupled with either emitter did not improve upon overall plate heat transfer rates obtained in baseline tests. On the contrary, heat transfer rates for individual plate sections were improved using the multipoint emitter and nozzle.